

CERN-EP-2016-228
19 Sep 2016

Evolution of the longitudinal and azimuthal structure of the near-side jet peak in Pb–Pb collisions at $\sqrt{s_{\text{NN}}} = 2.76$ TeV

ALICE Collaboration*

Abstract

In two-particle angular correlation measurements, jets give rise to a near-side peak, formed by particles associated to a higher p_{T} trigger particle. Measurements of these correlations as a function of pseudorapidity ($\Delta\eta$) and azimuthal ($\Delta\phi$) differences are used to extract the centrality and p_{T} dependence of the shape of the near-side peak in the p_{T} range $1 < p_{\text{T}} < 8$ GeV/ c in Pb–Pb and pp collisions at $\sqrt{s_{\text{NN}}} = 2.76$ TeV. A combined fit of the near-side peak and long-range correlations is applied to the data and the peak shape is quantified by the variance of the distributions. While the width of the peak in the $\Delta\phi$ direction is almost independent of centrality, a significant broadening in the $\Delta\eta$ direction is found from peripheral to central collisions. This feature is prominent for the low p_{T} region and vanishes above 4 GeV/ c . The widths measured in peripheral collisions are equal to those in pp in the $\Delta\phi$ direction and above 3 GeV/ c in the $\Delta\eta$ direction. Furthermore, for the 10% most central collisions and $1 < p_{\text{T,assoc}} < 2$ GeV/ c , $1 < p_{\text{T,trig}} < 3$ GeV/ c a departure from a Gaussian shape is found: a depletion develops around the centre of the peak. The results are compared to AMPT model simulations as well as other theoretical calculations indicating that the broadening and the development of the depletion is connected to the strength of radial and longitudinal flow.

© 2016 CERN for the benefit of the ALICE Collaboration.

Reproduction of this article or parts of it is allowed as specified in the CC-BY-4.0 license.

*See Appendix A for the list of collaboration members

1 Introduction

In elementary interactions with large momentum transfer ($Q^2 \gg \Lambda_{\text{QCD}}^2$), partons with high transverse momentum (p_T) are produced. Carrying net colour charge, they cannot exist freely and, instead, evolve from high to low virtuality producing parton showers. These eventually hadronize into a spray of collimated hadrons called jets. High- p_T partons are produced at the early stages of heavy-ion collisions. They propagate and evolve through the dense and hot medium created in these collisions and are expected to lose energy due to induced gluon radiation and elastic scatterings, a process commonly referred to as jet quenching. The transfer of energy from the leading parton to the medium and/or into additional gluon radiation leads to effects that can be exploited to characterise the colour density and scattering power of the medium.

Experimental methods to study high- p_T parton production differ in their capability to reconstruct the original parton momentum and to characterize the angular and momentum distribution of jet fragments. Furthermore, their sensitivity to experimental bias, most particularly the bias associated with the large underlying-event background encountered in heavy-ion collisions, is different. Inclusive hadron spectra are unbiased observables, mainly sensitive to the hadronic fragments with the largest momentum fraction (leading particles). Partonic energy loss suppresses high- p_T particle yields relative to their production in more elementary pp and p-A collisions which was observed at RHIC and LHC energies. The largest suppression is observed in central Pb-Pb collisions at the LHC at $p_T \approx 7$ GeV/c [1, 2].

Jet reconstruction algorithms have the objective to recombine a maximum of jet fragments within a certain area in the pseudorapidity (η) - azimuth (ϕ) plane in order to obtain the original parton energy and direction. In heavy-ion collisions, due to the large fluctuating energy from particles uncorrelated to the jets, the underlying event, jet reconstruction is limited to high transverse energy and small areas (cone-size) around the parton direction. An inclusive jet suppression commensurable to that of hadrons has been observed at the LHC [3–5] together with a large di-jet energy asymmetry [6, 7], suggesting that a large fraction of the lost energy is radiated outside the typical jet cone sizes of $R = 0.3$ – 0.5 . Detailed studies of the energy balance in events with high-energy jets show that the lost energy reappears primarily at low to intermediate p_T (0.5 – 3 GeV/c) outside the jet cone [7]. Studies of the momentum and angular distributions of jet fragments show that the jet core is almost unmodified [8–10].

Di-hadron angular correlations represent a powerful complementary tool to study jet quenching and the redistribution of energy in an energy region where jets cannot be identified event-by-event over the fluctuating background and where quenching effects are expected to be large. Such studies involve measuring the distributions of the relative azimuthal angle $\Delta\phi$ and pseudorapidity $\Delta\eta$ between particle pairs. The pairs consist of a trigger particle in a certain transverse momentum $p_{T,\text{trig}}$ interval and an associated particle in a $p_{T,\text{assoc}}$ interval. In these correlations, jets manifest themselves as a peak centred around ($\Delta\phi = 0$, $\Delta\eta = 0$) (near-side peak) and a structure elongated in $\Delta\eta$ at $\Delta\phi = \pi$ (the away-side or recoil-region). At low p_T , resonance decays as well as femtoscopic correlations also contribute to the near-side peak. The advantage of using di-hadron correlations is that an event-averaged subtraction of the background from particles uncorrelated to the jet can be performed. This advantage is shared with the analysis of hadron-jet correlations recently reported in Ref. [11, 12].

At RHIC, the near-side associated particle yield and peak shape have been studied for different systems and collision energies [13–15]. Small modifications of the yields with respect to a pp reference from PYTHIA are observed and there is remarkably little dependence on the collision system at the centre-of-mass energies of $\sqrt{s_{\text{NN}}} = 62.4$ and 200 GeV. An exception is the measurement in central Au-Au collisions at $\sqrt{s_{\text{NN}}} = 200$ GeV where the jet-like correlation is substantially broader and the momentum spectrum softer than in peripheral collisions and than those in collisions of other systems in this kinematic regime.

At the LHC, the measurement of the yield of particles associated to a high- p_T trigger particle (8–

15 GeV/c) in central Pb–Pb collisions relative to the pp reference at $p_{T,assoc} > 3$ GeV/c shows a suppression on the away-side and a moderate enhancement on the near-side indicating that medium-induced modifications can also be expected on the near side [16]. Much stronger modifications are observed for lower trigger and associated particle p_T ($3 < p_{T,trig} < 3.5$ GeV/c and $1 < p_{T,assoc} < 1.5$ GeV/c) [17, 18]. In the most central Pb–Pb collisions, the near-side yield is enhanced by a factor of 1.7.

The present paper expands these studies at the LHC to the characterisation of the angular distribution of the associated particles with respect to the trigger particle. The angular distribution is sensitive to the broadening of the jet due to the degradation of its energy and the distribution of radiated energy. Moreover, possible interactions of the parton shower with the collective longitudinal expansion [19–21] or with turbulent colour fields [22] in the medium would result in near-side peak shapes that are broader in the $\Delta\eta$ than in the $\Delta\phi$ direction. Results from the study of the near-side peak shape of charged particles as a function of centrality and for different combinations of trigger and associated particle p_T are discussed.

The paper is organised in the following way: the ALICE sub-systems used in the analysis are described in Section 2 and the data samples, event and track selection in Section 3. Section 4 describes the analysis methods and the systematic uncertainties are discussed in Section 5. Results are presented in Section 6 and conclusions are drawn in Section 7. The key results of the presented analysis are also reported in a short companion paper [23].

2 Experimental setup

A detailed description of the ALICE detector can be found in Ref. [24]. The main subsystems used in the present analysis are the Inner Tracking System (ITS) and the Time Projection Chamber (TPC). These have a common acceptance of $|\eta| < 0.9$ and are operated inside a solenoidal magnetic field of 0.5 T. The ITS consists of six layers of silicon detectors for vertex finding and tracking. The two outermost layers of the ITS constitute of the Silicon Strip Detectors (SSD), the two middle layers of the Silicon Drift Detectors (SDD) and the two innermost layers of the Silicon Pixel Detector (SPD) with the later also used for triggering. The TPC is the main tracking detector measuring up to 159 space points per track. The V0 detector, consisting of two arrays of 32 scintillator tiles each, and covering $2.8 < \eta < 5.1$ (V0-A) and $-3.7 < \eta < -1.7$ (V0-C), was used for triggering and centrality determination [25, 26]. All these detector systems have full azimuthal coverage.

Data from the 2010 and 2011 Pb–Pb runs of the LHC at $\sqrt{s_{NN}} = 2.76$ TeV and the 2011 pp run at the same energy are combined in the present analysis. From the 2010 sample, about 16 million minimum-bias Pb–Pb events are considered, while in the 2011 Pb–Pb run about 2 million minimum-bias events and about 21 million centrality-triggered events enhancing the 0–50% centrality range are used. The pp event sample consists of 30 million minimum-bias events.

In Pb–Pb collisions, the trigger required a coincidence of signals in both V0-A and V0-C. In addition, two Zero Degree Calorimeters (ZDCs) for neutron detection located at ± 114 m from the interaction point are used to suppress electromagnetic interactions. More details about the event selection can be found in Ref. [27]. The events are characterized into five collision-centrality classes based on the sum of amplitudes in the V0 detectors [26] (0–10% (most central), 10–20%, 20–30%, 30–50% and 50–80%). In pp collisions, the trigger required a signal in either of the V0 detectors or the SPD [28]. In both collision systems, these triggers are fully efficient for events entering the two-particle correlation analysis presented in this work.

3 Event and track selection

The collision-vertex position is determined with tracks reconstructed in the ITS and TPC as described in Ref. [1]. The vertex reconstruction algorithm is fully efficient for events with at least one reconstructed primary track within $|\eta| < 1.4$ [29]. The position of the reconstructed vertex along the beam direction (z_{vtx}) is required to be within 7 cm of the detector centre. This value is reduced to 3 cm in the study of systematic uncertainties.

The analysis uses tracks reconstructed in the ITS and TPC with $1 < p_T < 8 \text{ GeV}/c$ and in a fiducial region of $|\eta| < 0.8$. As a first step in the track selection, criteria on the number of space points (at least 70) and the quality of the track fit ($\chi^2/\text{ndf} < 2$) in the TPC are applied. Tracks are further required to have a distance of closest approach to the reconstructed vertex smaller than 2.4 cm and 3.2 cm in the transverse and the longitudinal direction, respectively. Two classes of tracks are combined in order to avoid an azimuthally-dependent tracking efficiency due to inactive SPD modules [30]. The first class requires for tracks to have at least one hit in the SPD. For tracks which do not fulfil this criterion, in the second class, the primary vertex position is used as additional constraint in the global track fit. An alternative track selection [31], where a tighter p_T -dependent cut on the distance of closest approach to the reconstructed vertex is applied, is used for the assignment of a systematic uncertainty. Further, the tracks in the second class are required to have a hit in the first layer of the SDD. This modified selection has a less uniform azimuthal acceptance, but includes a smaller number of secondary particles produced by interactions in the detector material or weak decays.

The efficiency and purity of the primary charged-particle selection are estimated from a Monte Carlo (MC) simulation using the HIJING 1.383 event generator [32] (for Pb–Pb) and the PYTHIA 6.4 event generator [33] with the tune Perugia-0 [34] (for pp) with particle transport through the detector carried out with GEANT3 [35]. The combined efficiency and acceptance of the track reconstruction in $|\eta| < 0.8$ is about 82–85% at $p_T = 1 \text{ GeV}/c$ and decreases to about 76–80% at $p_T = 8 \text{ GeV}/c$ depending on collision system, data sample and event centrality. The contamination from secondary particles resulting from weak decays and due to interactions in the detector material decreases from 2.5–4.5% to 0.5–1% in the p_T range from 1 to 8 GeV/c. The contribution from fake tracks, arising from improperly associated hits, is negligible. The alternative track selection (see above), has 3–6% lower combined efficiency and acceptance and about two thirds of the secondary contamination.

Due to the combination of different event samples, see Sec. 2, the number of accepted events per centrality class is not uniform, as is shown in Table 1.

4 Analysis

The correlation between two charged particles (denoted trigger and associated particle) is measured as a function of the azimuthal angle difference $\Delta\phi$ (defined within $-\pi/2$ and $3\pi/2$) and pseudorapidity difference $\Delta\eta$ [36]. The correlation is expressed in terms of the associated yield per trigger particle

| Collision system | Centrality class | Accepted events (10^6) |
|------------------|------------------|----------------------------|
| Pb–Pb | 0–10% | 7.7 |
| | 10–20% | 2.9 |
| | 20–30% | 2.9 |
| | 30–50% | 5.9 |
| | 50–80% | 3.9 |
| pp | — | 24.0 |

Table 1: Centrality classes and corresponding number of accepted events in pp and Pb–Pb collisions at $\sqrt{s_{\text{NN}}} = 2.76 \text{ TeV}$ used in this analysis.

for intervals of trigger and associated transverse momentum, $p_{T,\text{trig}}$ and $p_{T,\text{assoc}}$, respectively. The p_T intervals can be different or identical, in which case only pairs of particles with $p_{T,\text{assoc}} < p_{T,\text{trig}}$ are considered to avoid double counting. The per-trigger yield can be measured experimentally if the particle distribution is independent of pseudorapidity [37] in the following way:

$$\frac{1}{N_{\text{trig}}} \frac{d^2 N_{\text{assoc}}}{d\Delta\eta d\Delta\phi} = \frac{S(\Delta\eta, \Delta\phi)}{B(\Delta\eta, \Delta\phi)} \quad (1)$$

where N_{trig} is the total number of trigger particles in the centrality class and $p_{T,\text{trig}}$ interval, ranging from 0.18 to 36 per event. The signal distribution $S(\Delta\eta, \Delta\phi) = 1/N_{\text{trig}} d^2 N_{\text{same}}/d\Delta\eta d\Delta\phi$ is the associated yield per trigger particle for particle pairs from the same event. The background distribution $B(\Delta\eta, \Delta\phi) = \alpha d^2 N_{\text{mixed}}/d\Delta\eta d\Delta\phi$ corrects for finite pair acceptance and pair efficiency. It is constructed by correlating the trigger particles in one event with the associated particles from other events in the same centrality class and within the same 2 cm-wide z_{vtx} interval (each event is mixed with 5–20 events depending on the number of tracks per event). The background distribution is scaled by a factor α which is chosen such that $B(0, 0)$ is unity for pairs where both particles travel in approximately the same direction (i.e. $\Delta\phi \approx 0$, $\Delta\eta \approx 0$), and thus the efficiency and acceptance for the two particles are identical by construction. The yield defined by Eq. 1 is constructed for each z_{vtx} interval to account for differences in pair acceptance and efficiency, depending on the vertex position z_{vtx} . The trigger particles and the pairs are corrected for single-particle efficiency, described below, before the final per-trigger yield is obtained by calculating the average of the z_{vtx} intervals weighted by N_{trig} .

A minimum opening angle of the particle pairs is required for both signal and background to avoid a bias due to the reduced efficiency for pairs with small separation. Pairs are required to have a separation of $|\Delta\phi_{\text{min}}^*| > 0.02$ rad or $|\Delta\eta| > 0.02$, where $\Delta\phi_{\text{min}}^*$ is the minimal azimuthal distance at the same radius between the two tracks within the active detector volume after accounting for the bending in the magnetic field. Furthermore, correlations induced by secondary particles from long-lived neutral-particle decays (K_s^0 and Λ) and γ -conversions are suppressed by cutting on the invariant mass (m_{inv}) of the particle pair. Pairs are removed which are likely to stem from a γ -conversion ($m_{\text{inv}} < 4 \text{ MeV}/c^2$), a K_s^0 decay ($|m_{\text{inv}} - m(K_s^0)| < 5 \text{ MeV}/c^2$) or a Λ decay ($|m_{\text{inv}} - m(\Lambda)| < 5 \text{ MeV}/c^2$). Weak decays of heavier particles give a negligible contribution.

Each trigger and each associated particle is weighted with a correction factor that accounts for detector acceptance, reconstruction efficiencies and contamination from secondary particles. These corrections are applied as a function of η , p_T , z_{vtx} and event centrality. The shape parameters extracted below are expected to be insensitive to these single-particle corrections which was confirmed in the analysis.

The obtained per-trigger yields as a function of relative angle are integrated over particles produced within $|\eta| < 0.8$. As mentioned above, the method requires that the distribution of sources contributing to the correlation are independent of pseudorapidity, which is approximately the case for the inclusive particle distribution [25] as well as the anisotropic flow [38]. A dependence on pseudorapidity results in distortions as a function of $\Delta\eta$ of the per-trigger yields which are independent of $\Delta\phi$. In addition, the finite bin width in the event mixing has been found to cause $\Delta\eta$ -dependent effects. Distortions in $\Delta\eta$, of the order of 0.1%, have been observed and are attributed to the residual slight dependence of inclusive particle distribution and anisotropic flow on η . While small, these distortions are still relevant compared to the jet-like peak which is on top of the large combinatorial background. In order to suppress distortions of the peak in the $\Delta\eta$ direction, a correction factor is calculated such that the away side becomes independent of $\Delta\eta$ and is applied to all $\Delta\phi$ bins.

In order to characterize the near-side peak shape, a simultaneous fit of the peak, the combinatorial background and the long-range correlation background stemming from collective effects is performed. This exploits that in two-particle correlations the near-side peak is centred around $\Delta\phi = 0$, $\Delta\eta = 0$ while long-range correlation structures are approximately independent of $\Delta\eta$ [38]. This strategy limits the analysis

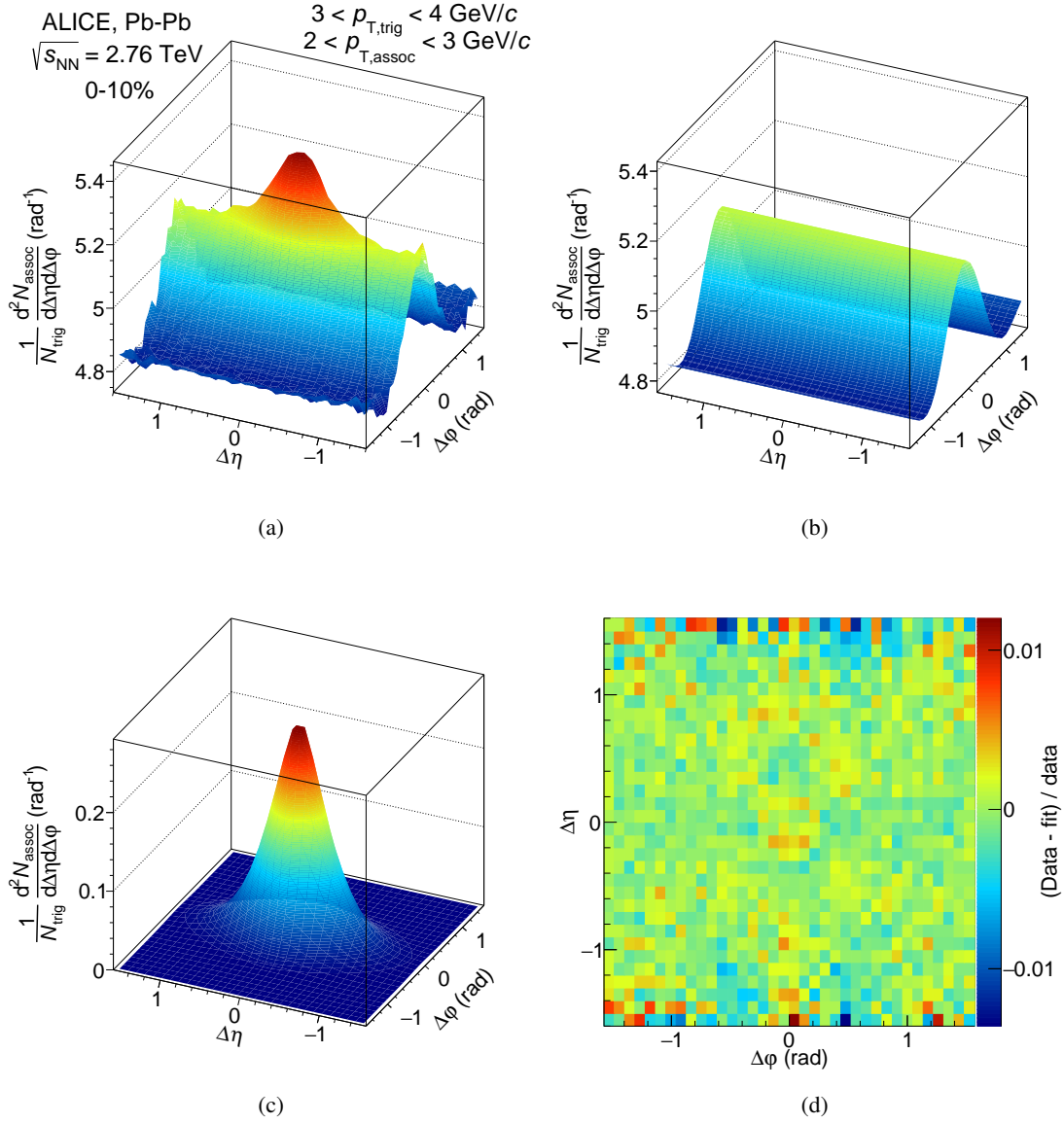


Fig. 1: Illustration of the fitting procedure for the 10% most central Pb–Pb events at $\sqrt{s_{\text{NN}}} = 2.76 \text{ TeV}$ in $2 < p_{\text{T,assoc}} < 3 \text{ GeV}/c$ and $3 < p_{\text{T,trig}} < 4 \text{ GeV}/c$. The panels show (a) the two-dimensional azimuthal and pseudorapidity total per-trigger yield, (b) the background distribution and (c) the signal peak component from the fit by Eq. 2, and (d) the relative difference between the data and the fit.

to the near side, as the away-side peak is elongated in $\Delta\eta$. The fit function used is a combination of a constant, a generalized two-dimensional Gaussian function and $\cos(n\Delta\phi)$ terms for $n = 2, 3, 4$.

$$F(\Delta\phi, \Delta\eta) = C_1 + \sum_{n=2}^4 2V_{n\Delta} \cos(n\Delta\phi) + C_2 \cdot G_{\gamma_{\Delta\phi}, w_{\Delta\phi}}(\Delta\phi) \cdot G_{\gamma_{\Delta\eta}, w_{\Delta\eta}}(\Delta\eta) \quad (2)$$

$$G_{\gamma_x, w_x}(x) = \frac{\gamma_x}{2w_x \Gamma(1/\gamma_x)} \exp \left[- \left(\frac{|x|}{w_x} \right)^{\gamma_x} \right] \quad (3)$$

Thus, in Pb–Pb collisions, the background is characterized by 4 parameters ($C_1, V_{n\Delta}$) where $V_{n\Delta}$ are the Fourier components of the long-range correlations [39], and it should be noted that the inclusion of orders higher than 4 does not significantly change the fit results. In pp collisions, however, the background consists effectively only of the pedestal C_1 . The peak magnitude is characterized by C_2 , and the shape which is the focus of the present analysis by 4 parameters ($\gamma_{\Delta\phi}, w_{\Delta\phi}, \gamma_{\Delta\eta}, w_{\Delta\eta}$). Note that for $\gamma = 2$

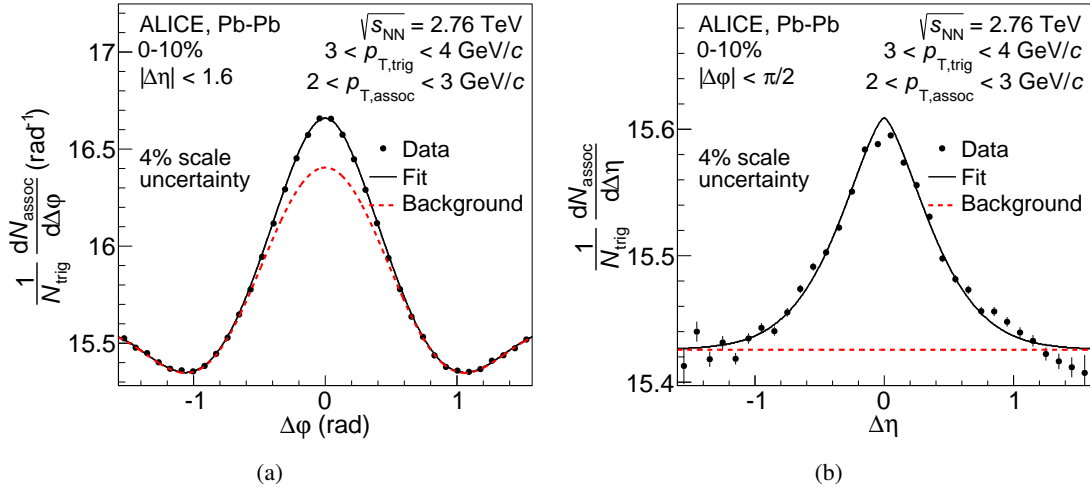


Fig. 2: Projections of Fig. 1 (a) to the $\Delta\phi$ (a) and $\Delta\eta$ (b) directions. The projections integrated over $|\Delta\eta| < 1.6$ and $|\Delta\phi| < \pi/2$, respectively, present per-trigger yields (and not densities) and therefore the level of the background is different than in Fig. 1. The fit and the background component of the fit are overlaid with the data.

the generalized Gaussian function G is a Gaussian, and for $\gamma = 1$ it is a Laplace distribution, which is an exponential where the absolute value of the argument is taken ($\exp(-|x|)$). The aim of using this fit function is to allow for a compact description of the data rather than attempting to give a physical meaning to each parameter. A further reduced description of the peak shape is provided by the variances ($\sigma_{\Delta\phi}$ and $\sigma_{\Delta\eta}$) of the generalized Gaussian. The evolution of the peak shape from peripheral to central collisions is described by the ratio of the width in the central bin (0–10%) and the peripheral bin (50–80%), denoted by $\sigma_{\Delta\phi}^{\text{CP}}$ and $\sigma_{\Delta\eta}^{\text{CP}}$.

In the data, a depletion around $\Delta\phi = 0$, $\Delta\eta = 0$ is observed at low p_T , however, the fit function does not include such a depletion. Several bins in the central region are excluded from the fit avoiding a bias on the extracted peak width. The size of the excluded region varies with p_T and centrality (from no exclusion to 0.3). Thus, by definition, the peak width describes the shape of the peak outside of the central region. The depletion in the central region is quantified by the near-side depletion yield in Section 6.3 by computing the difference between the fit and the per-trigger yield within the exclusion region.

Figure 1 illustrates the fit procedure. Shown is the data as well as the background and peak components of the fit. The bottom right panel shows the difference between the data and the fit where only minor deviations less than 0.5% can be observed. Figure 2 shows the $\Delta\phi$ and $\Delta\eta$ projections of the data overlaid with the obtained fit functions. The comparison with the background illustrates the magnitude of the peak.

In Pb–Pb collisions, the χ^2/ndf values of the fits are found in the range 1.0–2.5; most are around 1.5. In the highest two p_T bins (i.e. in $3 < p_{T,\text{assoc}} < 8 \text{ GeV}/c$ and $4 < p_{T,\text{trig}} < 8 \text{ GeV}/c$) the values increase up to about 2.5 showing that at high p_T the peak shape starts to depart from the generalized Gaussian description. In pp collisions, the χ^2/ndf values are in the range 1.3–2.0.

Different fitting strategies have been tried using a two-dimensional Gaussian to describe the peak, which is found to not describe the data satisfactorily (conversely, the χ^2/ndf is too large). A superposition of two two-dimensional Gaussians describes the data well, but is found unstable compared to the generalized Gaussian. In general, the fit with a single two-dimensional Gaussian results in smaller peak widths than the generalized Gaussian case which in turn has smaller peak widths than the two two-dimensional Gaussian fit.

| Source | $\sigma_{\Delta\phi}$ | $\sigma_{\Delta\eta}$ | $\sigma_{\Delta\phi}^{CP}$ | $\sigma_{\Delta\eta}^{CP}$ | Depletion yield |
|----------------------------------|-----------------------|-----------------------|----------------------------|----------------------------|-----------------|
| Track selection and efficiencies | 1.0% | | 1.3% | | 20% |
| Small opening angle cut | 0.7% | | 1.3% | | 5–10% |
| Neutral-particle decay cut | 0.1% | | 0.2% | | 8–20% |
| Vertex range | 1.0% | | 1.0% | | 5–10% |
| Pseudorapidity dependence | 1.7% | 4.1% | 0.6% | 2.5% | 5–15% |
| Exclusion region | 0.1% | 1.0% | 0.1% | 1.5% | 7–28% |
| Total | 2.3% | 4.5% | 2.2% | 3.6% | 24–45% |

Table 2: Summary of the systematic uncertainties of the analysis. Ranges indicate a dependence on centrality.

5 Systematic uncertainties

Systematic uncertainties connected to the measurement are determined modifying the selection criteria discussed above and repeating the analysis. The difference in the extracted parameters is studied as a function of p_T , centrality and collision system, but these dependencies are rather weak and one uncertainty value can be quoted for each source of systematic uncertainty in most cases. Finally, the contribution from the different sources of systematic uncertainties are added in quadrature. The extracted peak widths are rather insensitive to changes in the selections (total uncertainty of about 2–4.5%) while the near-side depletion yield defined in Sec. 6.3 is more sensitive (about 24–45% uncertainty).

Table 2 summarizes the different sources of systematic uncertainties which have been considered. Changes of vertex range and track selection have already been detailed in Sec. 3. The selection criterion on pairs with small opening angles (see Sec. 4) is increased by a factor 2 and the mass range in the cut removing neutral-particle decays is modified by 50%. The size of the exclusion region around $\Delta\phi = 0$, $\Delta\eta = 0$ (see Sec. 4) is enlarged by 0.17 (0.2) in the $\Delta\phi$ ($\Delta\eta$) direction. The sensitivity of the analysis results to the pseudorapidity range used is assessed by changing it by ± 0.1 . This uncertainty includes effects of the pseudorapidity dependence of the anisotropic flow as well as the particle production in general. No dependence of the results presented in this paper on the polarity of the magnetic field was observed.

The influence of resonance decays on the observations presented below were investigated by performing the analysis separately for like-sign and unlike-sign pairs. While the numerical values change, which is not unexpected, the qualitative conclusions presented below are unchanged. In particular, the reported broadening and depletion are larger in the like-sign case suggesting that resonance decays do not play a significant role for these phenomena.

6 Results

The top row of Fig. 3 shows the near-side peak in $1 < p_{T,\text{trig}} < 2 \text{ GeV}/c$ and $1 < p_{T,\text{assoc}} < 2 \text{ GeV}/c$ after subtraction of the background estimated with Eq. 2. The peak has a similar shape in pp collisions and in peripheral (50–80% centrality) Pb–Pb collisions, where it is approximately symmetric in $\Delta\phi$ and $\Delta\eta$. In the 10% most central collisions a different picture is observed: the near-side peak is broader than in peripheral collisions and wider in $\Delta\eta$ than in $\Delta\phi$. Furthermore, a depletion around $\Delta\phi = 0$, $\Delta\eta = 0$ develops which will be discussed in more detail further below. At higher p_T (bottom row of Fig. 3), the near-side peak is also found broader in central collisions than in peripheral or pp collisions, although it is visually less pronounced, but the asymmetry between $\Delta\phi$ and $\Delta\eta$ disappears at the two highest p_T bins included in the analysis. In addition, the amplitude of the peak is smaller in central collisions. Figure 4 shows the projections of the two-dimensional histogram shown in Fig. 3(c), where the depletion is largest, together with the fitted function.

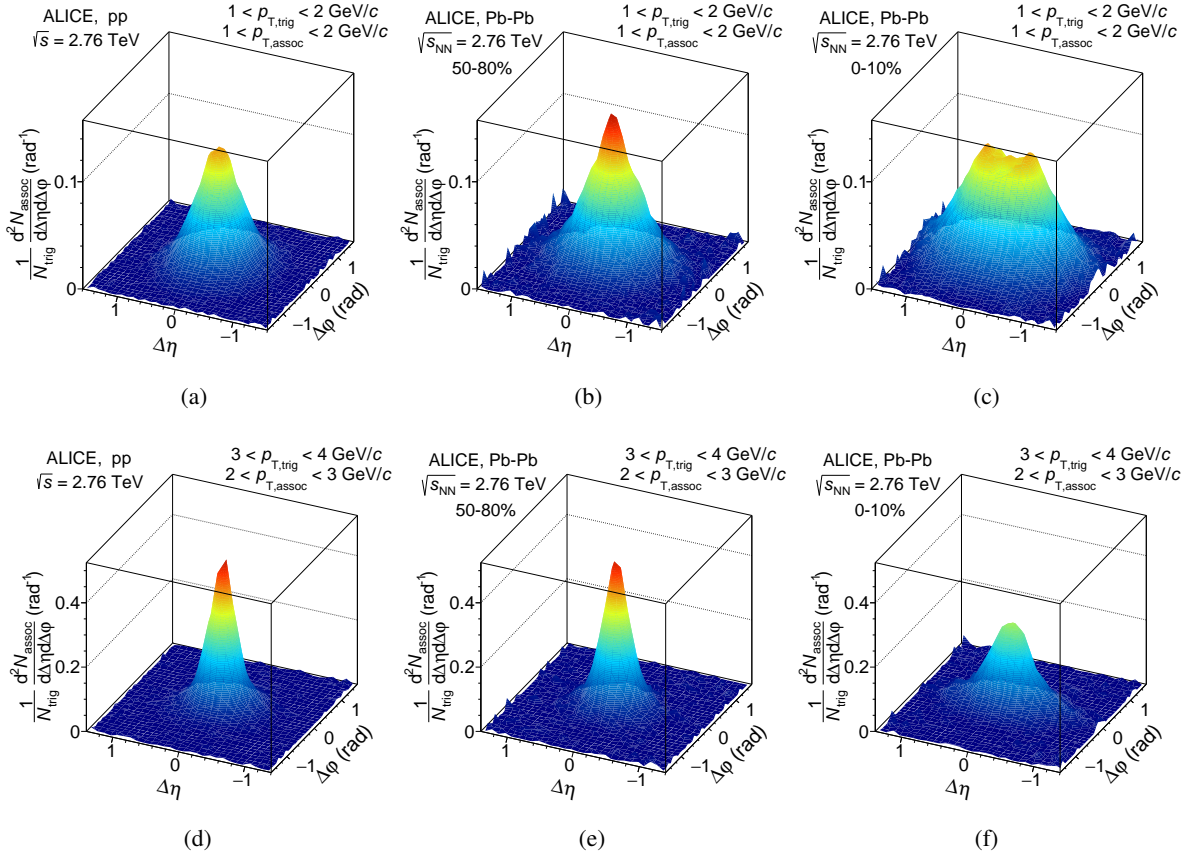


Fig. 3: Associated yield per trigger particle as a function of $\Delta\phi$ and $\Delta\eta$ in pp collisions (left panels) and Pb–Pb collisions at $\sqrt{s_{NN}} = 2.76$ TeV in the 50–80% centrality class (middle panels) and in the 0–10% centrality class (right panels). The top row shows $1 < p_{T,assoc} < 2$ GeV/c and $1 < p_{T,trig} < 2$ GeV/c and the bottom row shows $2 < p_{T,assoc} < 3$ GeV/c and $3 < p_{T,trig} < 4$ GeV/c. The background obtained from the fit function has been subtracted in order to emphasize the near-side peak.

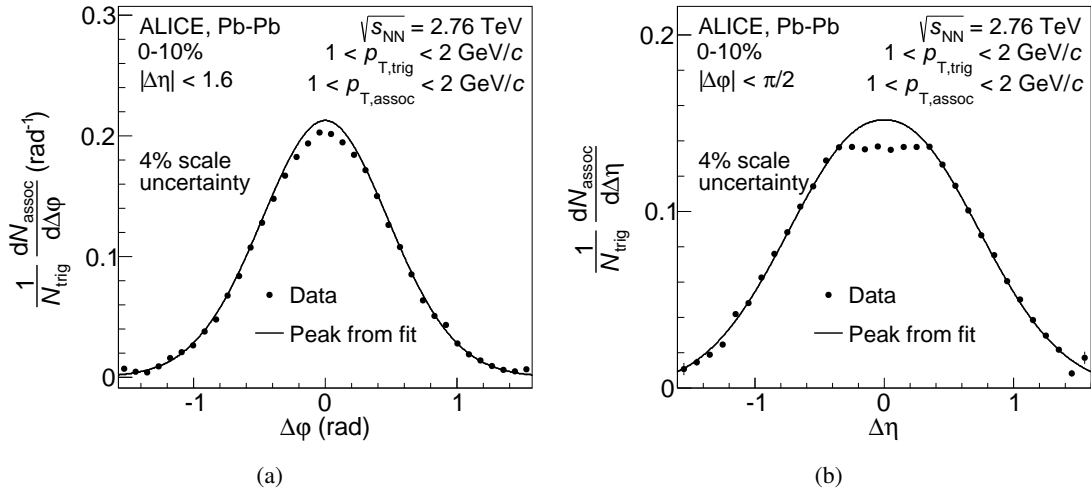


Fig. 4: Projections of Fig. 3(c) to the $\Delta\phi$ (a) and $\Delta\eta$ (b) directions, the depletion around $\Delta\phi = 0$, $\Delta\eta = 0$ is clearly visible in both directions.

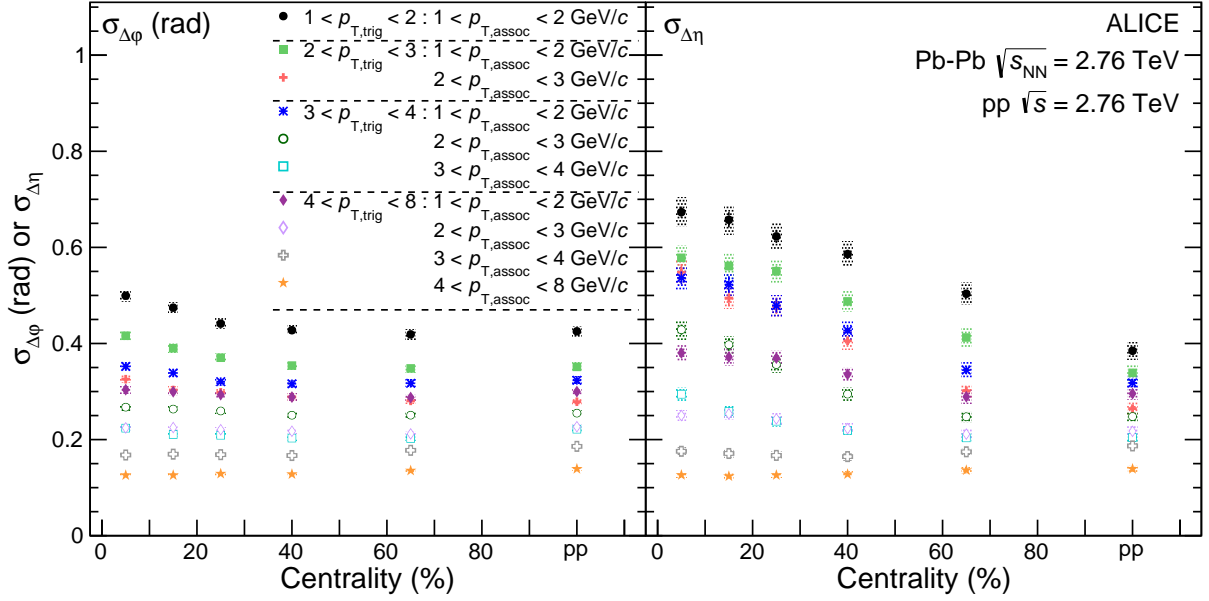


Fig. 5: Shape parameters $\sigma_{\Delta\phi}$ (left panel) and $\sigma_{\Delta\eta}$ (right panel) as a function of centrality in different p_T ranges for Pb–Pb collisions at $\sqrt{s_{NN}} = 2.76$ TeV and pp collisions (right most points in each panel). Lines indicate statistical uncertainties (mostly smaller than the marker size), while boxes denote systematic uncertainties. The markers are placed at the centre of the centrality bins.

6.1 Peak widths

We examine and quantify the evolution of the near-side peak shape and width with the fit procedure described in Sec. 4. The extracted shape parameters $\sigma_{\Delta\phi}$ and $\sigma_{\Delta\eta}$ are presented in Fig. 5. In pp collisions, the σ values range from 0.14 to 0.43 showing the expected p_T dependence: due to the boost of the evolving parton shower at larger p_T the peak is narrower. In the $\Delta\phi$ direction (left panel) the values obtained in pp collisions are consistent with those in peripheral Pb–Pb collisions. The peak width increases towards central events which is most pronounced in the lowest p_T bin (20% increase). In the higher p_T bins no significant width increase can be observed. In the $\Delta\eta$ direction (right panel) a much larger broadening towards central collisions is found. Already in peripheral collisions the width is larger than in pp collisions, and from peripheral to central collisions the width increases further up to $\sigma_{\Delta\eta} = 0.67$ in the lowest p_T bin. The largest relative increase of about 85% is observed for $2 < p_{T, \text{trig}} < 3$ GeV/c and $2 < p_{T, \text{assoc}} < 3$ GeV/c. A significant broadening can be observed for all but the two largest p_T bins. This increase is quantified for all p_T bins in Fig. 6 by $\sigma_{\Delta\phi}^{\text{CP}}$ and $\sigma_{\Delta\eta}^{\text{CP}}$. The increase is quantified with respect to peripheral Pb–Pb instead of pp to facilitate the MC comparisons discussed below.

In pp collisions, the peak shows circular symmetry in the $\Delta\eta$ – $\Delta\phi$ plane for all p_T . In Pb–Pb collisions, the peak becomes asymmetric towards central collisions for all but the two highest p_T bins. The magnitude of this asymmetry depends on p_T and is largest with about 70% ($\sigma_{\Delta\eta} > \sigma_{\Delta\phi}$) in the range $2 < p_{T, \text{trig}} < 3$ GeV/c and $2 < p_{T, \text{assoc}} < 3$ GeV/c.

6.2 Model comparison

The interplay of longitudinal flow with a fragmenting high p_T parton was suggested in Ref. [19] as a possible source for the observed asymmetric peak shape. The authors argue that hard partons are interacting with a medium which shows collective behaviour. This is confronted with the simpler picture where the parton propagates through an isotropic medium with respect to the parton direction. In their calculation the scattering centres are Lorentz-boosted by applying a momentum shift depending on the collective component transverse to the parton-propagation direction. The calculation in Ref. [19] for

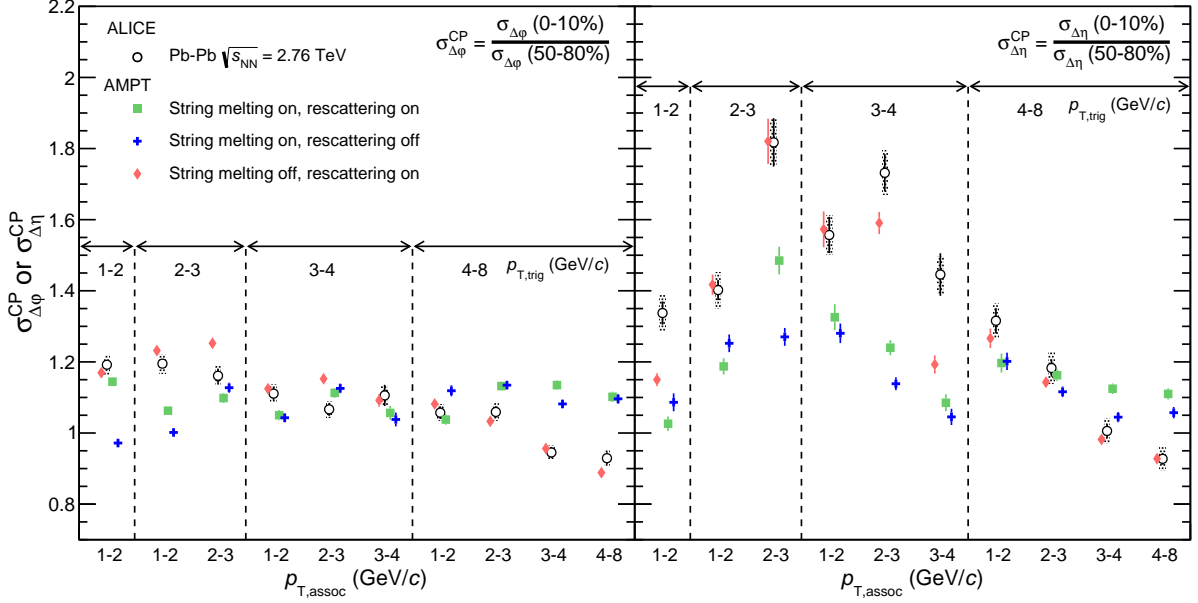


Fig. 6: Ratio of the peak widths in $\Delta\phi$ (left panel) and $\Delta\eta$ (right panel) observed in central (0–10%) and peripheral (50–80%) collisions as a function of $p_{T,\text{trigger}}$ and $p_{T,\text{assoc}}$ ranges. The data is compared to the different AMPT settings. Note that the x -axis combines the $p_{T,\text{assoc}}$ and $p_{T,\text{trigger}}$ axis, and therefore, a uniform trend of the values is not expected. Lines indicate statistical uncertainties (mostly smaller than the marker size), while boxes (only for data) denote systematic uncertainties.

Au–Au collisions at $\sqrt{s_{\text{NN}}} = 200$ GeV expects a 20% increase from peripheral to central events for the $\Delta\phi$ direction and a 60% increase for the $\Delta\eta$ direction. Despite the different centre-of-mass energy and collision system, the calculation is in quantitative agreement with the results presented in this paper.

Further studies on the possibility that the effect can be caused by an interplay of flow and jets have been done comparing the data to generator-level results from A Multi-Phase Transport model (AMPT) [40, 41] which has been shown to feature a longitudinal broadening of the near-side peak [42]. Two mechanisms in AMPT produce collective effects: partonic and hadronic rescattering. Before partonic rescattering, the initially produced strings may be broken into smaller pieces by the so-called string melting. Three different AMPT settings are considered, having either string melting or hadronic rescattering or both activated.¹ About 10 million events were generated for each of the cases with string melting activated, and about 47 million events for the case with string melting disabled. The results obtained in pp collisions are compared to PYTHIA 8.1 simulations [44] with the Monash tune [45] with about 500 million generated events.

The peak widths and $\sigma_{\Delta\phi}^{\text{CP}}$ and $\sigma_{\Delta\eta}^{\text{CP}}$ are extracted from particle level AMPT simulations in the same way as for the data. Figure 6 compares these ratios to the data. In the $\Delta\phi$ direction, the setting with string melting deactivated and hadronic rescattering active follows the trend of the data closest. The two other settings show a more uniform distribution across p_T and only differ in the two lowest p_T bins. In the $\Delta\eta$ direction, the setting with string melting deactivated and hadronic rescattering active quite remarkably follows the trend of the data including the large increase for intermediate p_T . The two other settings show qualitatively a similar trend but miss the data quantitatively.

In addition to the relative increase, it is interesting to compare the absolute widths. Figure 7 presents the ratio of the widths measured in Pb–Pb collisions to the three AMPT settings as well as the ones

¹AMPT versions v1.25t3 (without string melting, parameter isoft = 1) and v2.25t3 (with string melting, parameter isoft = 4) are used. In addition, in one sample the use of rescattering in the hadronic phase is disabled by setting the parameter nmax to 3 (the default is 150). See Ref. [43] for more details on these settings.

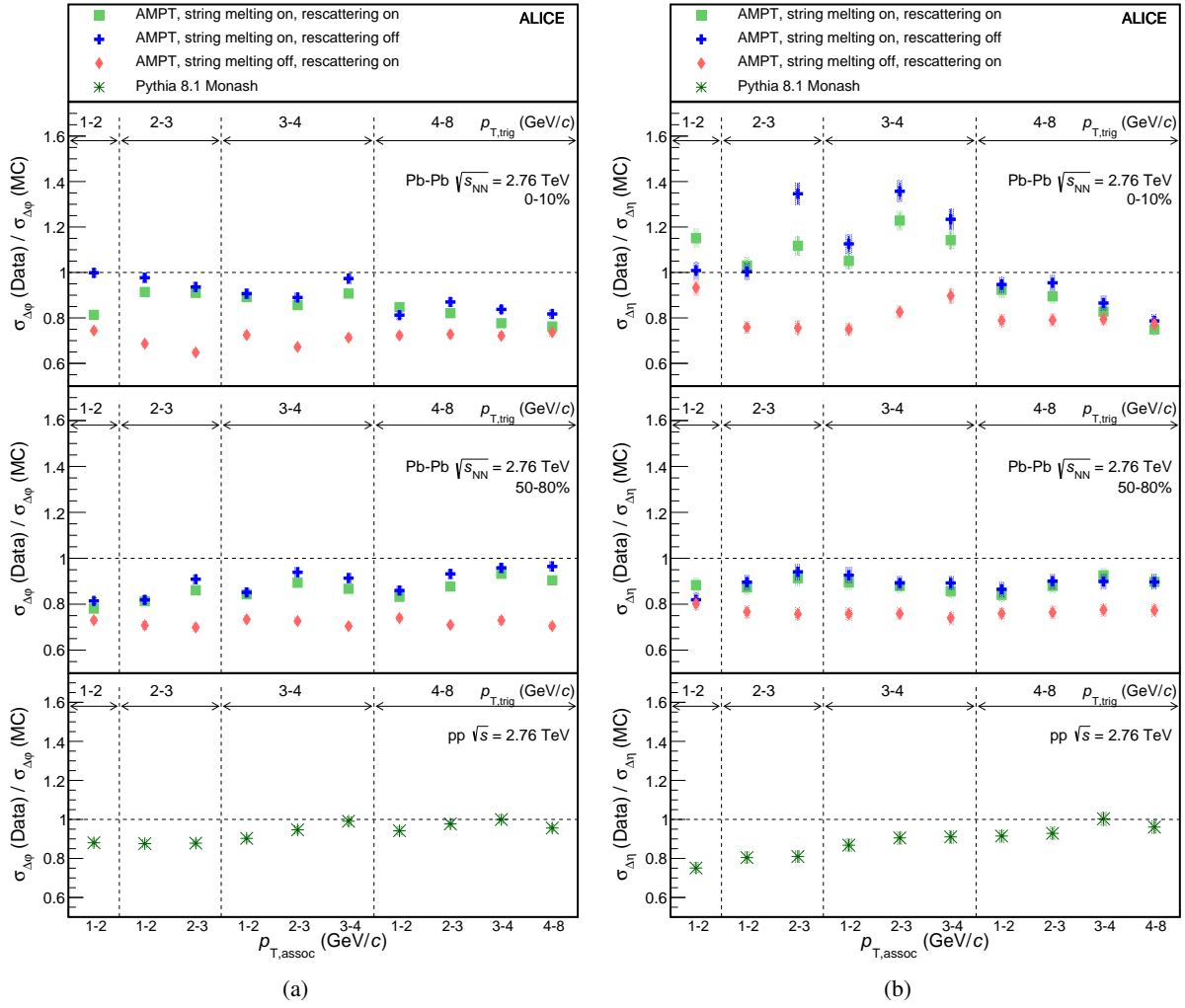


Fig. 7: Ratio of the peak widths in Pb–Pb collisions in central collisions (top panels) and peripheral collisions (centre panels) as well as in pp collisions to PYTHIA (bottom panels). Panel (a) show the shape parameters $\sigma_{\Delta\phi}$ while panel (b) show $\sigma_{\Delta\eta}$. Lines indicate statistical uncertainties (mostly smaller than the marker size), while boxes denote systematic uncertainties.

measured in pp collisions to PYTHIA simulations with the Monash tune. In general, none of the AMPT settings provides an accurate description of the data. The setting which matches best the relative width increase (string melting deactivated, hadronic rescattering active), overestimates the width by on average 20–30% with a mild p_T dependence. The two settings with string melting show a decreasing (increasing) trend as a function of p_T in central (peripheral) collisions in the $\Delta\phi$ direction. In the $\Delta\eta$ direction, in central collisions, they both over- and underestimate the data depending on p_T , while there is about 10% overestimation in peripheral collisions mostly independent of p_T . The width in pp collisions is well described by PYTHIA at high p_T in both directions, while the width in $\Delta\phi$ ($\Delta\eta$) is overestimated by 10% (25%) at low p_T .

6.3 Near-side depletion

The results presented in the previous section have focused on the overall shape of the near-side peak. In addition to the broadening, a distinct feature in central collisions and at the low p_T is observed, a depletion around $\Delta\phi = 0$, $\Delta\eta = 0$ (top right panel of Fig. 3 and Fig. 4).

An extensive set of studies was carried out to determine whether this depletion could arise from detector

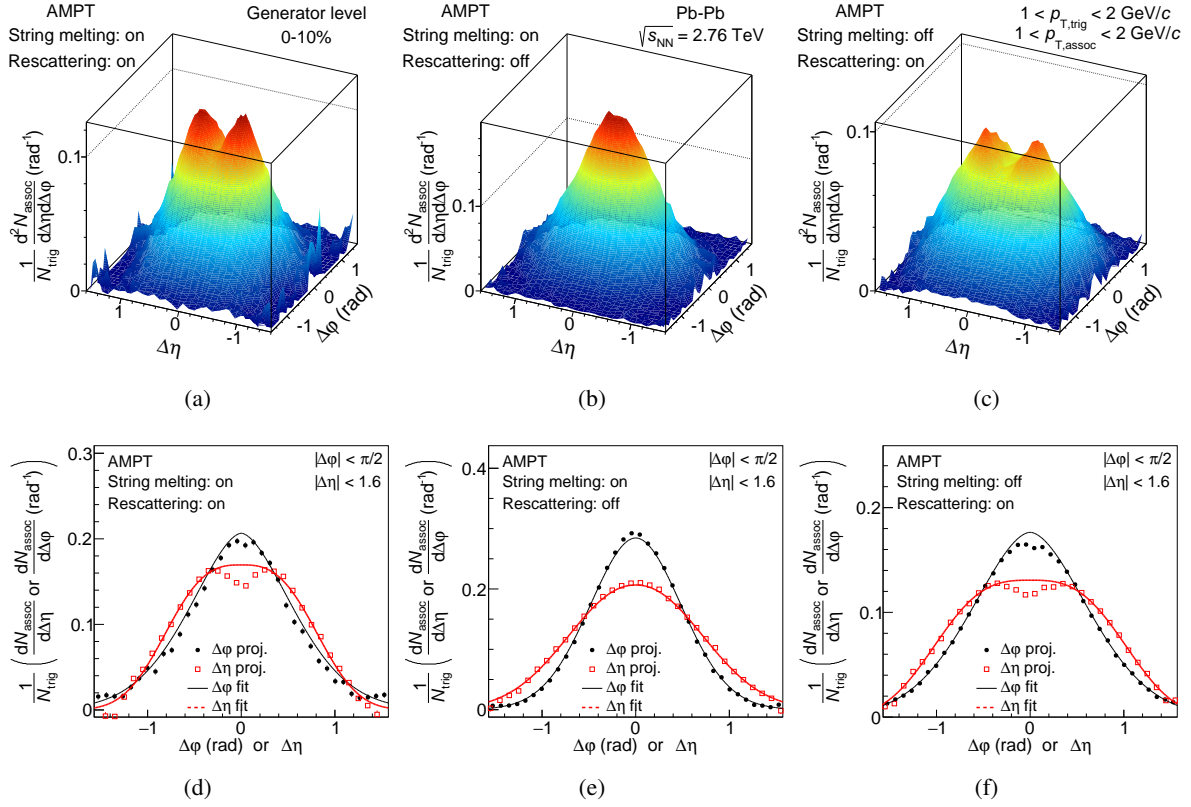


Fig. 8: Upper row: associated yield per trigger particle as a function of $\Delta\phi$ and $\Delta\eta$ in AMPT (generator level) for the 10% most central events. Lower row: projections to the $\Delta\phi$ and $\Delta\eta$ axis. The bin shown is $1 < p_{\text{T,trig}} < 2$ GeV/c and $1 < p_{\text{T,assoc}} < 2$ GeV/c. Three different AMPT settings are shown. Left panels: string melting and hadronic rescattering active; middle panels: only string melting active; right panels: only hadronic rescattering active. As in Fig. 3, the combinatorial and flow background has been subtracted using the fit function.

effects. Studies focused, in particular, on two-track effects: tracks with similar momenta which overlap in parts of the detector volume may suffer from efficiency losses and reconstruction imperfections, e.g. a splitting of a particle's trajectory into two tracks may cause distortions of the two-particle correlation around $\Delta\phi = 0$, $\Delta\eta = 0$. It was shown that such detector-related effects are present but only in a very limited region of where both $|\Delta\phi|$ and $|\Delta\eta|$ are smaller than 0.04–0.05. The depletion discussed in this section extends out to $|\Delta\eta|$ well beyond 0.3 which is significantly larger than the detector resolution and the reach of two-track efficiency effects. A detector-related origin is thus excluded.

Figure 8 presents the per-trigger yield and their projections to the $\Delta\phi$ and $\Delta\eta$ axes for the AMPT simulations in the same p_{T} and centrality bin as the top panel of Fig. 3. The AMPT simulations with hadronic rescattering show a depletion regardless of the string melting setting.

In order to quantify this depletion, the difference between the fit (where the depletion region has been excluded, see above) and the per-trigger yield relative to the total peak yield for the p_{T} bins is computed and this is referred to as depletion yield in the following. The region where effects are expected from the limited two-track reconstruction efficiency ($|\Delta\phi| < 0.04$ and $|\Delta\eta| < 0.05$, which corresponds to 0.5–6% of the integrated region) is excluded from this calculation. Fig. 9 presents the depletion yield as a function of centrality for the p_{T} bins where it is different from 0. It can be seen that $(2.2 \pm 0.5)\%$ of the yield is missing in the lowest p_{T} bin ($1 < p_{\text{T,trig}} < 2$ GeV/c, $1 < p_{\text{T,assoc}} < 2$ GeV/c) and in the 10% most central events. This value decreases gradually with centrality and with p_{T} . No significant depletion is observed for 50–80% (30–80%) centrality or pp collisions for the lowest (second lowest) p_{T} range. For higher p_{T} bins, no significant depletion is observed.

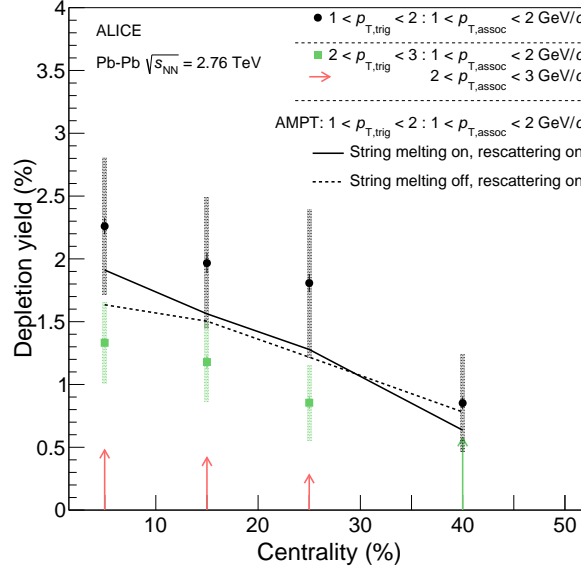


Fig. 9: Missing yield in the depletion region relative to the overall peak yield extracted from the fit. Lines indicate statistical uncertainties (mostly smaller than the marker size), while boxes (only for data) denote systematic uncertainties. The arrows indicate the upper limit in case the uncertainty bands touch 0. The markers are placed at the centre of the centrality bins. For comparison, the non-zero values from two AMPT simulations are shown as lines.

The depletion observed in the AMPT events is present only in the lowest p_T bin, where its value is compatible with the data for both settings where hadronic rescattering is switched on. For larger p_T bins and for the configuration without hadronic rescattering the depletion yield is consistent with 0 in AMPT.

6.4 Relation to radial and elliptic flow

In order to put the observations in context with the strength of radial and anisotropic flow, Table 3 presents the radial-flow expansion velocity β_T and the elliptic flow coefficient $v_2\{2\}$ for the 10% most central events from data (from [46, 47]) and from the AMPT samples. The expansion velocity β_T is extracted from a Blast-Wave fit to the p_T -spectra of π , K and p in the range of $0.5 < p_T < 1$ GeV/c, $0.2 < p_T < 1.5$ GeV/c and $0.3 < p_T < 2$ GeV/c, respectively, and in the rapidity range of $|y| < 0.5$. The fit describes the AMPT simulation with 10% precision in the fitted range (see Ref. [46] for details on the fitting procedure). The $v_2\{2\}$ is extracted from two-particle correlations within $|\eta| < 0.8$ and $0.2 < p_T < 5$ GeV/c (see Ref. [47] for details on the procedure).

| Sample | β_T | $v_2\{2\}$ |
|---|-------------------|---------------------|
| AMPT string melting and hadronic rescattering | 0.442 | 0.0412 ± 0.0002 |
| AMPT string melting | 0.202 | 0.0389 ± 0.0002 |
| AMPT hadronic rescattering | 0.540 | 0.0330 ± 0.0002 |
| Data | 0.649 ± 0.022 | 0.0364 ± 0.0003 |

Table 3: Blast-wave fit parameter β_T and elliptic flow coefficient $v_2\{2\}$ for 0–10% centrality in Pb–Pb collisions at $\sqrt{s_{NN}} = 2.76$ TeV in the considered AMPT samples and for comparison in the data (from [46, 47]). Uncertainties are statistical for the MC samples and combined statistical and systematic ones for the data. The statistical uncertainties for the Blast-wave fits on AMPT are negligible.

The radial-flow expansion velocity β_T is larger when hadronic rescattering is active and largest if in addition string melting is switched off, while the configuration without hadronic rescattering results in a low β_T . The value found in the data is about 20% larger than the highest one in the AMPT simulations. The elliptic flow coefficient $v_2\{2\}$ is better described by AMPT. Closest are the configurations

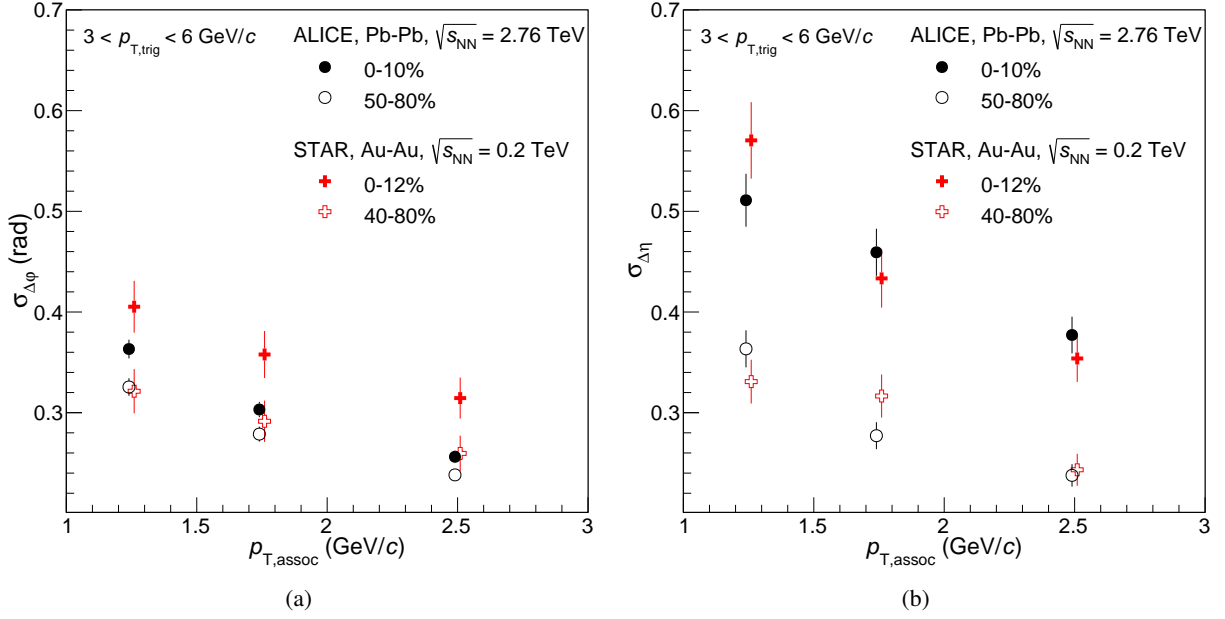


Fig. 10: Comparison of the shape parameters $\sigma_{\Delta\phi}$ (left panel) and $\sigma_{\Delta\eta}$ (right panel) to results from the STAR collaboration in Au–Au collisions at $\sqrt{s_{\text{NN}}} = 200\text{ GeV}$ [14]. The markers are placed at the centre of the $p_{\text{T,assoc}}$ bins, slightly displaced for visibility, and the uncertainties are statistical and systematic ones added in quadrature.

with either string melting or hadronic rescattering (about 7% discrepancy), while the configuration with both processes simultaneously overestimates the $v_2\{2\}$. The differences between the different AMPT configurations are much smaller for the elliptic flow than for the radial flow.

The depletion discussed in the previous section occurs in the two AMPT configurations where the β_{T} is large, while the configuration without the depletion has the smallest β_{T} . The coefficient $v_2\{2\}$ has significantly different values in the two configurations with depletion, and the relative increase of the peak width (Fig. 6) is best described by the AMPT configuration with the largest β_{T} . These studies suggest that the radial flow is more likely responsible for the depletion than the elliptic flow.

Ref. [42] studied partonic pseudorapidity distributions at different evolution times in AMPT. The authors show that the longitudinal broadening is driven by large values of longitudinal flow. In a picture where expansion is driven by pressure gradients, strong radial expansion can be accompanied by large longitudinal expansion. In conclusion, in AMPT, the observed phenomena are related to large values of radial and longitudinal flow.

6.5 Comparison to other experiments

The STAR collaboration has studied near-side peak shapes at $\sqrt{s_{\text{NN}}} = 62.4\text{ GeV}$ and $\sqrt{s_{\text{NN}}} = 200\text{ GeV}$ in d+Au, Cu–Cu and Au–Au collisions [14]. Apart from the peak width quantification, done separately in the $\Delta\eta$ and $\Delta\phi$ direction with one-dimensional Gaussian functions after the subtraction of the background, the analysis method is compatible to the one presented in this analysis. In the studies presented in this paper, it was found that the peak widths with one two-dimensional Gaussian lead generally to smaller values than with the generalized Gaussian, and the fit quality is not optimal for the large statistics collected at the LHC. However, despite the difference in centre-of-mass energy, the larger statistical uncertainties in the analysis reported by the STAR collaboration may have hidden the possibility that the generalized Gaussian is a better description of the near-side peak.

The STAR collaboration also observed a broadening of the peak widths from peripheral to central collisions at $\sqrt{s_{\text{NN}}} = 200\text{ GeV}$ in Au–Au collisions. The effect is most significant for $2 < p_{\text{T,assoc}} < 4\text{ GeV}/c$.

In the $\Delta\phi$ direction, the width increases by 25–30% depending on the p_T , and in the $\Delta\eta$ direction, the increase is about 40–60%. This effect is comparable to the observations presented in this paper. Figure 10 compares the results in the centrality bins which have the largest overlap between the two experiments. Agreement between the STAR results and this work is observed, within statistical uncertainties, in all overlapping momentum and centrality bins, with the exception of central collisions in the $\Delta\phi$ direction, where a two-sigma difference can be seen.

7 Summary

We have presented a detailed characterization of the flow-subtracted near-side peak in two-particle correlations in Pb–Pb collisions at $\sqrt{s_{NN}} = 2.76$ TeV together with a measurement in pp collisions at the same energy. The near-side peak shows the characteristic p_T dependence, where the width decreases with increasing p_T . In addition, in Pb–Pb collisions a centrality dependence is observed: the peak gets wider from peripheral to central collisions. This effect is significantly stronger for the $\Delta\eta$ direction than for the $\Delta\phi$ direction leading to an asymmetric peak shape in central collisions, observed over a wide p_T range. Additionally, at low p_T , an unexpected depletion develops from peripheral to central collisions.

AMPT simulations show that both the asymmetric broadening and the depletion are also present when hadronic rescattering is included. The AMPT configuration with hadronic rescattering and without string melting reproduces quantitatively the relative peak broadening as well as the size of the depletion. The extraction of the radial-flow expansion velocity suggests that the stronger the radial flow, the stronger the observed effects are. In addition, earlier theoretical and phenomenological work connected the longitudinal broadening of the near-side jet-like peak to strong longitudinal flow in AMPT, as well as to an interplay of partons traversing the longitudinally expanding medium. Thus a possible scenario is that the presented observations are caused by the interplay of the jet with the collective expansion.

Acknowledgements

The ALICE Collaboration would like to thank all its engineers and technicians for their invaluable contributions to the construction of the experiment and the CERN accelerator teams for the outstanding performance of the LHC complex. The ALICE Collaboration gratefully acknowledges the resources and support provided by all Grid centres and the Worldwide LHC Computing Grid (WLCG) collaboration. The ALICE Collaboration acknowledges the following funding agencies for their support in building and running the ALICE detector: A. I. Alikhanyan National Science Laboratory (Yerevan Physics Institute) Foundation (ANSL), State Committee of Science and World Federation of Scientists (WFS), Armenia; Austrian Academy of Sciences and Nationalstiftung für Forschung, Technologie und Entwicklung, Austria; , Conselho Nacional de Desenvolvimento Científico e Tecnológico (CNPq), Financiadora de Estudos e Projetos (Finep) and Fundação de Amparo à Pesquisa do Estado de São Paulo (FAPESP), Brazil; Ministry of Education of China (MOE of China), Ministry of Science & Technology of China (MOST of China) and National Natural Science Foundation of China (NSFC), China; Ministry of Science, Education and Sport and Croatian Science Foundation, Croatia; Centro de Investigaciones Energéticas, Medioambientales y Tecnológicas (CIEMAT), Cuba; Ministry of Education, Youth and Sports of the Czech Republic, Czech Republic; Danish National Research Foundation (DNRF), The Carlsberg Foundation and The Danish Council for Independent Research — Natural Sciences, Denmark; Helsinki Institute of Physics (HIP), Finland; Commissariat à l’Energie Atomique (CEA) and Institut National de Physique Nucléaire et de Physique des Particules (IN2P3) and Centre National de la Recherche Scientifique (CNRS), France; Bundesministerium für Bildung, Wissenschaft, Forschung und Technologie (BMBF) and GSI Helmholtzzentrum für Schwerionenforschung GmbH, Germany; Ministry of Education, Research and Religious Affairs, Greece; National Research, Development and Innovation Office, Hungary; Department of Atomic

Energy Government of India (DAE), India; Indonesian Institute of Science, Indonesia; Centro Fermi - Museo Storico della Fisica e Centro Studi e Ricerche Enrico Fermi and Istituto Nazionale di Fisica Nucleare (INFN), Italy; Institute for Innovative Science and Technology , Nagasaki Institute of Applied Science (IIST), Japan Society for the Promotion of Science (JSPS) KAKENHI and Japanese Ministry of Education, Culture, Sports, Science and Technology (MEXT), Japan; Consejo Nacional de Ciencia (CONACYT) y Tecnología, through Fondo de Cooperación Internacional en Ciencia y Tecnología (FONCICYT) and Dirección General de Asuntos del Personal Académico (DGAPA), Mexico; Nationaal instituut voor subatomaire fysica (Nikhef), Netherlands; The Research Council of Norway, Norway; Commission on Science and Technology for Sustainable Development in the South (COMSATS), Pakistan; Pontificia Universidad Católica del Perú, Peru; Ministry of Science and Higher Education and National Science Centre, Poland; Ministry of Education and Scientific Research, Institute of Atomic Physics and Romanian National Agency for Science, Technology and Innovation, Romania; Joint Institute for Nuclear Research (JINR), Ministry of Education and Science of the Russian Federation and National Research Centre Kurchatov Institute, Russia; Ministry of Education, Science, Research and Sport of the Slovak Republic, Slovakia; National Research Foundation of South Africa, South Africa; Korea Institute of Science and Technology Information and National Research Foundation of Korea (NRF), South Korea; Centro de Investigaciones Energéticas, Medioambientales y Tecnológicas (CIEMAT) and Ministerio de Ciencia e Innovación, Spain; Knut & Alice Wallenberg Foundation (KAW) and Swedish Research Council (VR), Sweden; European Organization for Nuclear Research, Switzerland; National Science and Technology Development Agency (NSDTA), Office of the Higher Education Commission under NRU project of Thailand and Suranaree University of Technology (SUT), Thailand; Turkish Atomic Energy Agency (TAEK), Turkey; National Academy of Sciences of Ukraine, Ukraine; Science and Technology Facilities Council (STFC), United Kingdom; National Science Foundation of the United States of America (NSF) and United States Department of Energy, Office of Nuclear Physics (DOE NP), United States.

References

- [1] **ALICE** Collaboration, B. Abelev *et al.*, “Centrality Dependence of Charged Particle Production at Large Transverse Momentum in Pb–Pb Collisions at $\sqrt{s_{NN}} = 2.76$ TeV,” *Phys. Lett.* **B720** (2013) 52–62, arXiv:1208.2711 [hep-ex].
- [2] **CMS** Collaboration, S. Chatrchyan *et al.*, “Study of high-pT charged particle suppression in PbPb compared to *pp* collisions at $\sqrt{s_{NN}} = 2.76$ TeV,” *Eur. Phys. J.* **C72** (2012) 1945, arXiv:1202.2554 [nucl-ex].
- [3] **ATLAS** Collaboration, G. Aad *et al.*, “Measurement of the jet radius and transverse momentum dependence of inclusive jet suppression in lead-lead collisions at $\sqrt{s_{NN}} = 2.76$ TeV with the ATLAS detector,” *Phys. Lett.* **B719** (2013) 220–241, arXiv:1208.1967 [hep-ex].
- [4] **ALICE** Collaboration, B. Abelev *et al.*, “Measurement of charged jet suppression in Pb-Pb collisions at $\sqrt{s_{NN}} = 2.76$ TeV,” *JHEP* **03** (2014) 013, arXiv:1311.0633 [nucl-ex].
- [5] **ALICE** Collaboration, J. Adam *et al.*, “Measurement of jet suppression in central Pb-Pb collisions at $\sqrt{s_{NN}} = 2.76$ TeV,” *Phys. Lett.* **B746** (2015) 1–14, arXiv:1502.01689 [nucl-ex].
- [6] **ATLAS** Collaboration, G. Aad *et al.*, “Observation of a Centrality-Dependent Dijet Asymmetry in Lead-Lead Collisions at $\sqrt{s_{NN}} = 2.77$ TeV with the ATLAS Detector at the LHC,” *Phys. Rev. Lett.* **105** (2010) 252303, arXiv:1011.6182 [hep-ex].
- [7] **CMS** Collaboration, S. Chatrchyan *et al.*, “Observation and studies of jet quenching in PbPb collisions at nucleon-nucleon center-of-mass energy = 2.76 TeV,” *Phys. Rev.* **C84** (2011) 024906, arXiv:1102.1957 [nucl-ex].

- [8] **CMS** Collaboration, S. Chatrchyan *et al.*, “Measurement of jet fragmentation into charged particles in pp and PbPb collisions at $\sqrt{s_{NN}} = 2.76$ TeV,” *JHEP* **1210** (2012) 087, arXiv:1205.5872 [nucl-ex].
- [9] **CMS** Collaboration, S. Chatrchyan *et al.*, “Measurement of jet fragmentation in PbPb and pp collisions at $\sqrt{s_{NN}} = 2.76$ TeV,” *Phys. Rev.* **C90** (2014) 024908, arXiv:1406.0932 [nucl-ex].
- [10] **ATLAS** Collaboration, G. Aad *et al.*, “Measurement of inclusive jet charged-particle fragmentation functions in Pb+Pb collisions at $\sqrt{s_{NN}} = 2.76$ TeV with the ATLAS detector,” *Phys. Lett.* **B739** (2014) 320–342, arXiv:1406.2979 [hep-ex].
- [11] **ALICE** Collaboration, J. Adam *et al.*, “Measurement of jet quenching with semi-inclusive hadron-jet distributions in central Pb-Pb collisions at $\sqrt{s_{NN}} = 2.76$ TeV,” *JHEP* **09** (2015) 170, arXiv:1506.03984 [nucl-ex].
- [12] **CMS** Collaboration, V. Khachatryan *et al.*, “Correlations between jets and charged particles in PbPb and pp collisions at $\sqrt{s_{NN}} = 2.76$ TeV,” *JHEP* **02** (2016) 156, arXiv:1601.00079 [nucl-ex].
- [13] **STAR** Collaboration, B. I. Abelev *et al.*, “Long range rapidity correlations and jet production in high energy nuclear collisions,” *Phys. Rev.* **C80** (2009) 064912, arXiv:0909.0191 [nucl-ex].
- [14] **STAR** Collaboration, G. Agakishiev *et al.*, “System size and energy dependence of near-side di-hadron correlations,” *Phys. Rev.* **C85** (2012) 014903, arXiv:1110.5800 [nucl-ex].
- [15] **STAR** Collaboration, L. Adamczyk *et al.*, “Jet-Hadron Correlations in $\sqrt{s_{NN}} = 200$ GeV $p + p$ and Central $Au + Au$ Collisions,” *Phys. Rev. Lett.* **112** (2014) 122301, arXiv:1302.6184 [nucl-ex].
- [16] **ALICE** Collaboration, K. Aamodt *et al.*, “Particle-yield modification in jet-like azimuthal di-hadron correlations in Pb-Pb collisions at $\sqrt{s_{NN}} = 2.76$ TeV,” *Phys. Rev. Lett.* **108** (2012) 092301, arXiv:1110.0121 [nucl-ex].
- [17] **CMS** Collaboration, S. Chatrchyan *et al.*, “Centrality dependence of dihadron correlations and azimuthal anisotropy harmonics in Pb–Pb collisions at $\sqrt{s_{NN}} = 2.76$ TeV,” *Eur. Phys. J.* **C72** (2012) 2012, arXiv:1201.3158 [nucl-ex].
- [18] **ALICE** Collaboration, J. Adam *et al.*, “Jet-like correlations with neutral pion triggers in pp and central Pb-Pb collisions at 2.76 TeV,” arXiv:1608.07201 [nucl-ex].
- [19] N. Armesto, C. A. Salgado, and U. A. Wiedemann, “Measuring the collective flow with jets,” *Phys. Rev. Lett.* **93** (2004) 242301, arXiv:hep-ph/0405301.
- [20] N. Armesto, C. A. Salgado, and U. A. Wiedemann, “Low-p(T) collective flow induces high-p(T) jet quenching,” *Phys. Rev.* **C72** (2005) 064910, arXiv:hep-ph/0411341 [hep-ph].
- [21] P. Romatschke, “Momentum broadening in an anisotropic plasma,” *Phys. Rev.* **C75** (2007) 014901, arXiv:hep-ph/0607327 [hep-ph].
- [22] A. Majumder, B. Muller, and S. A. Bass, “Longitudinal Broadening of Quenched Jets in Turbulent Color Fields,” *Phys. Rev. Lett.* **99** (2007) 042301, arXiv:hep-ph/0611135 [hep-ph].
- [23] **ALICE** Collaboration, J. Adam *et al.*, “Short version of this paper,” *Phys. Rev. Lett.* .
- [24] **ALICE** Collaboration, K. Aamodt *et al.*, “The ALICE experiment at the CERN LHC,” *JINST* **3** (2008) S08002.

- [25] ALICE Collaboration, K. Aamodt *et al.*, “Charged-particle multiplicity density at mid-rapidity in central Pb-Pb collisions at $\sqrt{s_{NN}} = 2.76$ TeV,” *Phys. Rev. Lett.* **105** (2010) 252301, arXiv:1011.3916 [nucl-ex].
- [26] ALICE Collaboration, B. Abelev *et al.*, “Centrality determination of Pb-Pb collisions at $\sqrt{s_{NN}} = 2.76$ TeV with ALICE,” *Phys. Rev.* **C88** (2013) 044909, arXiv:1301.4361 [nucl-ex].
- [27] ALICE Collaboration, K. Aamodt *et al.*, “Centrality dependence of the charged-particle multiplicity density at mid-rapidity in Pb-Pb collisions at $\sqrt{s_{NN}} = 2.76$ TeV,” *Phys. Rev. Lett.* **106** (2011) 032301, arXiv:1012.1657 [nucl-ex].
- [28] ALICE Collaboration, B. Abelev *et al.*, “Measurement of inelastic, single- and double-diffraction cross sections in proton–proton collisions at the LHC with ALICE,” *Eur. Phys. J.* **C73** (2013) 2456, arXiv:1208.4968 [hep-ex].
- [29] ALICE Collaboration, B. B. Abelev *et al.*, “Performance of the ALICE Experiment at the CERN LHC,” *Int. J. Mod. Phys.* **A29** (2014) 1430044, arXiv:1402.4476 [nucl-ex].
- [30] ALICE Collaboration, B. Abelev *et al.*, “Measurement of event background fluctuations for charged particle jet reconstruction in Pb–Pb collisions at $\sqrt{s_{NN}} = 2.76$ TeV,” *JHEP* **1203** (2012) 053, arXiv:1201.2423 [hep-ex].
- [31] ALICE Collaboration, B. Abelev *et al.*, “Underlying event measurements in pp collisions at $\sqrt{s} = 0.9$ and 7 TeV with the ALICE experiment at the LHC,” *JHEP* **1207** (2012) 116, arXiv:1112.2082 [hep-ex].
- [32] X.-N. Wang and M. Gyulassy, “HIJING: A Monte Carlo model for multiple jet production in pp, pA and AA collisions,” *Phys. Rev.* **D44** (1991) 3501.
- [33] T. Sjostrand, S. Mrenna, and P. Z. Skands, “PYTHIA 6.4 physics and manual,” *JHEP* **0605** (2006) 026, arXiv:hep-ph/0603175 [hep-ph].
- [34] P. Z. Skands, “Tuning Monte Carlo generators: The Perugia tunes,” *Phys. Rev.* **D82** (2010) 074018, arXiv:1005.3457 [hep-ph].
- [35] R. Brun *et al.*, “Geant detector description and simulation tool,” *CERN Program Library Long Write-up, W5013* (1994).
- [36] ALICE Collaboration, B. Abelev *et al.*, “Long-range angular correlations on the near and away side in p–Pb collisions at $\sqrt{s_{NN}}=5.02$ TeV,” *Phys. Lett.* **B719** (2013) 29–41, arXiv:1212.2001 [nucl-ex].
- [37] S. Ravan, P. Pujahari, S. Prasad, and C. A. Pruneau, “Correcting Correlation Function Measurements,” *Phys. Rev.* **C89** (2014) 024906, arXiv:1311.3915 [nucl-ex].
- [38] ALICE Collaboration, J. Adam *et al.*, “Pseudorapidity dependence of the anisotropic flow of charged particles in Pb-Pb collisions at $\sqrt{s_{NN}} = 2.76$ TeV,” *Physics Letters B* (2016), arXiv:1605.02035 [nucl-ex].
- [39] ALICE Collaboration, K. Aamodt *et al.*, “Harmonic decomposition of two-particle angular correlations in Pb–Pb collisions at $\sqrt{s_{NN}} = 2.76$ TeV,” *Phys. Lett.* **B708** (2012) 249–264, arXiv:1109.2501 [nucl-ex].
- [40] Z.-W. Lin, C. M. Ko, B.-A. Li, B. Zhang, and S. Pal, “A Multi-phase transport model for relativistic heavy ion collisions,” *Phys. Rev.* **C72** (2005) 064901, arXiv:nucl-th/0411110 [nucl-th].

- [41] J. Xu and C. M. Ko, “Pb-Pb collisions at $\sqrt{s_{NN}} = 2.76$ TeV in a multiphase transport model,” *Phys. Rev.* **C83** (2011) 034904, arXiv:1101.2231 [nucl-th].
- [42] G. L. Ma, S. Zhang, Y. G. Ma, X. Z. Cai, J. H. Chen, and C. Zhong, “Longitudinal broadening of near side jets due to parton cascade,” *Eur. Phys. J.* **C57** (2008) 589–593, arXiv:0807.3987 [nucl-th].
- [43] ALICE Collaboration, J. Adam *et al.*, “Higher harmonic flow coefficients of identified hadrons in Pb-Pb collisions at $\sqrt{s_{NN}} = 2.76$ TeV,” arXiv:1606.06057 [nucl-ex].
- [44] T. Sjostrand, S. Mrenna, and P. Z. Skands, “A Brief Introduction to PYTHIA 8.1,” *Comput. Phys. Commun.* **178** (2008) 852–867, arXiv:0710.3820 [hep-ph].
- [45] P. Skands, S. Carrazza, and J. Rojo, “Tuning PYTHIA 8.1: the Monash 2013 Tune,” *Eur. Phys. J.* **C74** (2014) 3024, arXiv:1404.5630 [hep-ph].
- [46] ALICE Collaboration, B. Abelev *et al.*, “Centrality dependence of π , K, p production in Pb-Pb collisions at $\sqrt{s_{NN}} = 2.76$ TeV,” *Phys. Rev.* **C88** (2013) 044910, arXiv:1303.0737 [hep-ex].
- [47] ALICE Collaboration, K. Aamodt *et al.*, “Elliptic flow of charged particles in Pb+Pb collisions at 2.76 TeV,” *Phys. Rev. Lett.* **105** (2010) 252302, arXiv:1011.3914 [nucl-ex].

A The ALICE Collaboration

J. Adam³⁹, D. Adamová⁸⁶, M.M. Aggarwal⁹⁰, G. Aglieri Rinella³⁵, M. Agnello^{113,31}, N. Agrawal⁴⁸, Z. Ahammed¹³⁷, S. Ahmad¹⁸, S.U. Ahn⁷⁰, S. Aiola¹⁴¹, A. Akhmedov⁵⁵, S.N. Alam¹³⁷, D.S.D. Albuquerque¹²⁴, D. Aleksandrov⁸², B. Alessandro¹¹³, D. Alexandre¹⁰⁴, R. Alfaro Molina⁶⁵, A. Alici^{107,12}, A. Alkin³, J. Alme^{22,37}, T. Alt⁴², S. Altinpinar²², I. Altsybeev¹³⁶, C. Alves Garcia Prado¹²³, M. An⁷, C. Andrei⁸⁰, H.A. Andrews¹⁰⁴, A. Andronic¹⁰⁰, V. Anguelov⁹⁶, C. Anson⁸⁹, T. Antičić¹⁰¹, F. Antinori¹¹⁰, P. Antonioli¹⁰⁷, R. Anwar¹²⁶, L. Aphecetche¹¹⁶, H. Appelshäuser⁶¹, S. Arcelli²⁷, R. Arnaldi¹¹³, O.W. Arnold^{97,36}, I.C. Arsene²¹, M. Arslandok⁶¹, B. Audurier¹¹⁶, A. Augustinus³⁵, R. Averbeck¹⁰⁰, M.D. Azmi¹⁸, A. Badalà¹⁰⁹, Y.W. Baek⁶⁹, S. Bagnasco¹¹³, R. Bailhache⁶¹, R. Bala⁹³, S. Balasubramanian¹⁴¹, A. Baldisseri¹⁵, R.C. Baral⁵⁸, A.M. Barbano²⁶, R. Barbera²⁸, F. Barile³³, G.G. Barnaföldi¹⁴⁰, L.S. Barnby^{104,35}, V. Barret⁷², P. Bartalini⁷, K. Barth³⁵, J. Bartke^{120,i}, E. Bartsch⁶¹, M. Basile²⁷, N. Bastid⁷², S. Basu¹³⁷, B. Bathen⁶², G. Batigne¹¹⁶, A. Batista Camejo⁷², B. Batyunya⁶⁸, P.C. Batzing²¹, I.G. Bearden⁸³, H. Beck⁹⁶, C. Bedda³¹, N.K. Behera⁵¹, I. Belikov⁶⁶, F. Bellini²⁷, H. Bello Martinez², R. Bellwied¹²⁶, L.G.E. Beltran¹²², V. Belyaev⁷⁷, G. Bencedi¹⁴⁰, S. Beole²⁶, A. Bercuci⁸⁰, Y. Berdnikov⁸⁸, D. Berenyi¹⁴⁰, R.A. Bertens^{54,129}, D. Berzano³⁵, L. Betev³⁵, A. Bhasin⁹³, I.R. Bhat⁹³, A.K. Bhati⁹⁰, B. Bhattacharjee⁴⁴, J. Bhom¹²⁰, L. Bianchi¹²⁶, N. Bianchi⁷⁴, C. Bianchin¹³⁹, J. Bielčák³⁹, J. Bielčiková⁸⁶, A. Bilandzic^{36,97}, G. Biro¹⁴⁰, R. Biswas⁴, S. Biswas^{81,4}, S. Bjelogrić⁵⁴, J.T. Blair¹²¹, D. Blau⁸², C. Blume⁶¹, F. Bock^{96,76}, A. Bogdanov⁷⁷, L. Boldizsár¹⁴⁰, M. Bombara⁴⁰, M. Bonora³⁵, J. Book⁶¹, H. Borel¹⁵, A. Borissov⁹⁹, M. Borri¹²⁸, E. Botta²⁶, C. Bourjau⁸³, P. Braun-Munzinger¹⁰⁰, M. Bregant¹²³, T.A. Broker⁶¹, T.A. Browning⁹⁸, M. Broz³⁹, E.J. Brucken⁴⁶, E. Bruna¹¹³, G.E. Bruno³³, D. Budnikov¹⁰², H. Buesching⁶¹, S. Bufalino^{26,31}, P. Buhler¹¹⁵, S.A.I. Buitron⁶³, P. Buncic³⁵, O. Busch¹³², Z. Buthelezi⁶⁷, J.B. Butt¹⁶, J.T. Buxton¹⁹, J. Cabala¹¹⁸, D. Caffarri³⁵, H. Caines¹⁴¹, A. Caliva⁵⁴, E. Calvo Villar¹⁰⁵, P. Camerini²⁵, F. Carena³⁵, W. Carena³⁵, F. Carnesecchi^{27,12}, J. Castillo Castellanos¹⁵, A.J. Castro¹²⁹, E.A.R. Casula²⁴, C. Ceballos Sanchez⁹, J. Cepila³⁹, P. Cerello¹¹³, J. Cerkala¹¹⁸, B. Chang¹²⁷, S. Chapeland³⁵, M. Chartier¹²⁸, J.L. Charvet¹⁵, S. Chattopadhyay¹³⁷, S. Chattopadhyay¹⁰³, A. Chauvin^{36,97}, V. Chelnokov³, M. Cherney⁸⁹, C. Cheshkov¹³⁴, B. Cheynis¹³⁴, V. Chibante Barroso³⁵, D.D. Chinellato¹²⁴, S. Cho⁵¹, P. Chochula³⁵, K. Choi⁹⁹, M. Chojnacki⁸³, S. Choudhury¹³⁷, P. Christakoglou⁸⁴, C.H. Christensen⁸³, P. Christiansen³⁴, T. Chujo¹³², S.U. Chung⁹⁹, C. Cicalo¹⁰⁸, L. Cifarelli^{12,27}, F. Cindolo¹⁰⁷, J. Cleymans⁹², F. Colamaria³³, D. Colella^{35,56}, A. Collu⁷⁶, M. Colocci²⁷, G. Conesa Balbastre⁷³, Z. Conesa del Valle⁵², M.E. Connors^{141,ii}, J.G. Contreras³⁹, T.M. Cormier⁸⁷, Y. Corrales Morales¹¹³, I. Cortés Maldonado², P. Cortese³², M.R. Cosentino^{125,123}, F. Costa³⁵, J. Crkovská⁵², P. Crochet⁷², R. Cruz Albino¹¹, E. Cuautle⁶³, L. Cunqueiro^{35,62}, T. Dahms^{36,97}, A. Dainese¹¹⁰, M.C. Danisch⁹⁶, A. Danu⁵⁹, D. Das¹⁰³, I. Das¹⁰³, S. Das⁴, A. Dash⁸¹, S. Dash⁴⁸, S. De^{123,49}, A. De Caro³⁰, G. de Cataldo¹⁰⁶, C. de Conti¹²³, J. de Cuveland⁴², A. De Falco²⁴, D. De Gruttola^{30,12}, N. De Marco¹¹³, S. De Pasquale³⁰, R.D. De Souza¹²⁴, A. Deisting^{100,96}, A. Deloff⁷⁹, C. Deplano⁸⁴, P. Dhankher⁴⁸, D. Di Bari³³, A. Di Mauro³⁵, P. Di Nezza⁷⁴, B. Di Ruzza¹¹⁰, M.A. Diaz Corchero¹⁰, T. Dietel⁹², P. Dillenseger⁶¹, R. Divià³⁵, Ø. Djuvsland²², A. Dobrin^{84,35}, D. Domenicis Gimenez¹²³, B. Dönigus⁶¹, O. Dordic²¹, T. Drozhzhova⁶¹, A.K. Dubey¹³⁷, A. Dubla¹⁰⁰, L. Ducroux¹³⁴, A.K. Duggal⁹⁰, P. Dupieux⁷², R.J. Ehlers¹⁴¹, D. Elia¹⁰⁶, E. Endress¹⁰⁵, H. Engel⁶⁰, E. Epple¹⁴¹, B. Erasmus¹¹⁶, F. Erhardt¹³³, B. Espagnon⁵², S. Esumi¹³², G. Eulisse³⁵, J. Eum⁹⁹, D. Evans¹⁰⁴, S. Evdokimov¹¹⁴, G. Eyyubova³⁹, L. Fabbietti^{36,97}, D. Fabris¹¹⁰, J. Faivre⁷³, A. Fantoni⁷⁴, M. Fasel^{76,87}, L. Feldkamp⁶², A. Feliciello¹¹³, G. Feofilov¹³⁶, J. Ferencei⁸⁶, A. Fernández Téllez², E.G. Ferreira¹⁷, A. Ferretti²⁶, A. Festanti²⁹, V.J.G. Feuillard^{72,15}, J. Figiel¹²⁰, M.A.S. Figueredo¹²³, S. Filchagin¹⁰², D. Finogeev⁵³, F.M. Fionda²⁴, E.M. Fiore³³, M. Floris³⁵, S. Foertsch⁶⁷, P. Foka¹⁰⁰, S. Fokin⁸², E. Fragiaco¹¹², A. Francescon³⁵, A. Francisco¹¹⁶, U. Frankenfeld¹⁰⁰, G.G. Fronze²⁶, U. Fuchs³⁵, C. Furget⁷³, A. Furs⁵³, M. Fusco Girard³⁰, J.J. Gaardhøje⁸³, M. Gagliardi²⁶, A.M. Gago¹⁰⁵, K. Gajdosova⁸³, M. Gallio²⁶, C.D. Galvan¹²², D.R. Gangadharan⁷⁶, P. Ganoti^{35,91}, C. Gao⁷, C. Garabatos¹⁰⁰, E. Garcia-Solis¹³, K. Garg²⁸, P. Garg⁴⁹, C. Gargiulo³⁵, P. Gasik^{36,97}, E.F. Gauger¹²¹, M.B. Gay Ducati⁶⁴, M. Germain¹¹⁶, P. Ghosh¹³⁷, S.K. Ghosh⁴, P. Gianotti⁷⁴, P. Giubellino^{113,35}, P. Giubilato²⁹, E. Gladysz-Dziadus¹²⁰, P. Glässel⁹⁶, D.M. Gómez Coral⁶⁵, A. Gomez Ramirez⁶⁰, A.S. Gonzalez³⁵, V. Gonzalez¹⁰, P. González-Zamora¹⁰, S. Gorbunov⁴², L. Görlich¹²⁰, S. Gotovac¹¹⁹, V. Grabski⁶⁵, L.K. Graczykowski¹³⁸, K.L. Graham¹⁰⁴, L. Greiner⁷⁶, A. Grelli⁵⁴, C. Grigoras³⁵, V. Grigoriev⁷⁷, A. Grigoryan¹, S. Grigoryan⁶⁸, N. Grión¹¹², J.M. Gronefeld¹⁰⁰, J.F. Grosse-Oetringhaus³⁵, R. Grosso¹⁰⁰, L. Gruber¹¹⁵, F. Guber⁵³, R. Guernane^{35,73}, B. Guerzoni²⁷, K. Gulbrandsen⁸³, T. Gunji¹³¹, A. Gupta⁹³, R. Gupta⁹³, I.B. Guzman², R. Haake^{35,62}, C. Hadjidakis⁵², H. Hamagaki^{131,78}, G. Hamar¹⁴⁰, J.C. Hamon⁶⁶, J.W. Harris¹⁴¹, A. Harton¹³, D. Hatzifotiadou¹⁰⁷, S. Hayashi¹³¹, S.T. Heckel⁶¹, E. Hellbär⁶¹, H. Helstrup³⁷, A. Hergehelegiu⁸⁰, G. Herrera Corral¹¹, F. Herrmann⁶², B.A. Hess⁹⁵, K.F. Hetland³⁷, H. Hillemanns³⁵, B. Hippolyte⁶⁶, J. Hladky⁵⁷, D. Horak³⁹, R. Hosokawa¹³², P. Hristov³⁵, C. Hughes¹²⁹, T.J. Humanic¹⁹, N. Hussain⁴⁴, T. Hussain¹⁸, D. Hutter⁴², D.S. Hwang²⁰, R. Ilkaev¹⁰², M. Inaba¹³²,

M. Ippolitov^{82,77}, M. Irfan¹⁸, V. Isakov⁵³, M.S. Islam⁴⁹, M. Ivanov^{100,35}, V. Ivanov⁸⁸, V. Izucheev¹¹⁴,
 B. Jacak⁷⁶, N. Jacazio²⁷, P.M. Jacobs⁷⁶, M.B. Jadhav⁴⁸, S. Jadlovská¹¹⁸, J. Jádlovský¹¹⁸, C. Jahnke^{123,36},
 M.J. Jakubowska¹³⁸, M.A. Janik¹³⁸, P.H.S.Y. Jayarathna¹²⁶, C. Jena⁸¹, S. Jena¹²⁶, R.T. Jimenez Bustamante¹⁰⁰,
 P.G. Jones¹⁰⁴, A. Jusko¹⁰⁴, P. Kalinak⁵⁶, A. Kalweit³⁵, J.H. Kang¹⁴², V. Kaplin⁷⁷, S. Kar¹³⁷, A. Karasu Uysal⁷¹,
 O. Karavichev⁵³, T. Karavicheva⁵³, L. Karayan^{100,96}, E. Karpechev⁵³, U. Kebschull⁶⁰, R. Keidel¹⁴³,
 D.L.D. Keijdener⁵⁴, M. Keil³⁵, M. Mohisin Khan^{18,iii}, P. Khan¹⁰³, S.A. Khan¹³⁷, A. Khanzadeev⁸⁸,
 Y. Kharlov¹¹⁴, A. Khatun¹⁸, A. Khuntia⁴⁹, B. Kileng³⁷, D.W. Kim⁴³, D.J. Kim¹²⁷, D. Kim¹⁴², H. Kim¹⁴²,
 J.S. Kim⁴³, J. Kim⁹⁶, M. Kim⁵¹, M. Kim¹⁴², S. Kim²⁰, T. Kim¹⁴², S. Kirsch⁴², I. Kisel⁴², S. Kiselev⁵⁵,
 A. Kisiel¹³⁸, G. Kiss¹⁴⁰, J.L. Klay⁶, C. Klein⁶¹, J. Klein³⁵, C. Klein-Bösing⁶², S. Klewin⁹⁶, A. Kluge³⁵,
 M.L. Knichel⁹⁶, A.G. Knospe^{121,126}, C. Kobdaj¹¹⁷, M. Kofarago³⁵, T. Kollegger¹⁰⁰, A. Kolojvari¹³⁶,
 V. Kondratiev¹³⁶, N. Kondratyeva⁷⁷, E. Kondratyuk¹¹⁴, A. Konevskikh⁵³, M. Kopcik¹¹⁸, M. Kour⁹³,
 C. Kouzinopoulos³⁵, O. Kovalenko⁷⁹, V. Kovalenko¹³⁶, M. Kowalski¹²⁰, G. Koyithatta Meethalevedu⁴⁸,
 I. Králik⁵⁶, A. Kravčáková⁴⁰, M. Krivda^{56,104}, F. Krizek⁸⁶, E. Kryshen^{35,88}, M. Krzewicki⁴², A.M. Kubera¹⁹,
 V. Kučera⁸⁶, C. Kuhn⁶⁶, P.G. Kuijjer⁸⁴, A. Kumar⁹³, J. Kumar⁴⁸, L. Kumar⁹⁰, S. Kumar⁴⁸, S. Kundu⁸¹,
 P. Kurashvili⁷⁹, A. Kurepin⁵³, A.B. Kurepin⁵³, A. Kuryakin¹⁰², S. Kushpil⁸⁶, M.J. Kweon⁵¹, Y. Kwon¹⁴²,
 S.L. La Pointe⁴², P. La Rocca²⁸, C. Lagana Fernandes¹²³, I. Lakomov³⁵, R. Langoy⁴¹, K. Lapidus^{36,141},
 C. Lara⁶⁰, A. Lardeux¹⁵, A. Lattuca²⁶, E. Laudi³⁵, L. Lazaridis³⁵, R. Lea²⁵, L. Leardini⁹⁶, S. Lee¹⁴², F. Lehas⁸⁴,
 S. Lehner¹¹⁵, J. Lehrbach⁴², R.C. Lemmon⁸⁵, V. Lenti¹⁰⁶, E. Leogrande⁵⁴, I. León Monzón¹²², P. Lévai¹⁴⁰,
 S. Li⁷, X. Li¹⁴, J. Lien⁴¹, R. Lietava¹⁰⁴, S. Lindal²¹, V. Lindenstruth⁴², C. Lippmann¹⁰⁰, M.A. Lisa¹⁹,
 H.M. Ljunggren³⁴, W. Llope¹³⁹, D.F. Lodato⁵⁴, P.I. Loenne²², V. Loginov⁷⁷, C. Loizides⁷⁶, X. Lopez⁷²,
 E. López Torres⁹, A. Lowe¹⁴⁰, P. Luettig⁶¹, M. Lunardon²⁹, G. Luparello²⁵, M. Lupi³⁵, T.H. Lutz¹⁴¹,
 A. Maevskaya⁵³, M. Mager³⁵, S. Mahajan⁹³, S.M. Mahmood²¹, A. Maire⁶⁶, R.D. Majka¹⁴¹, M. Malaev⁸⁸,
 I. Maldonado Cervantes⁶³, L. Malinina^{68,iv}, D. Mal'Kevich⁵⁵, P. Malzacher¹⁰⁰, A. Mamonov¹⁰², V. Manko⁸²,
 F. Manso⁷², V. Manzari¹⁰⁶, Y. Mao⁷, M. Marchisone^{130,67}, J. Mareš⁵⁷, G.V. Margagliotti²⁵, A. Margotti¹⁰⁷,
 J. Margutti⁵⁴, A. Marín¹⁰⁰, C. Markert¹²¹, M. Marquard⁶¹, N.A. Martin¹⁰⁰, P. Martinengo³⁵, M.I. Martínez²,
 G. Martínez García¹¹⁶, M. Martinez Pedreira³⁵, A. Mas¹²³, S. Masciocchi¹⁰⁰, M. Maserà²⁶, A. Masoni¹⁰⁸,
 A. Mastroserio³³, A. Matyja^{129,120}, C. Mayer¹²⁰, J. Mazer¹²⁹, M. Mazzilli³³, M.A. Mazzoni¹¹¹, F. Meddi²³,
 Y. Melikyan⁷⁷, A. Menchaca-Rocha⁶⁵, E. Meninno³⁰, J. Mercado Pérez⁹⁶, M. Meres³⁸, S. Mhlanga⁹²,
 Y. Miake¹³², M.M. Mieskolainen⁴⁶, K. Mikhaylov^{55,68}, L. Milano⁷⁶, J. Milosevic²¹, A. Mischke⁵⁴,
 A.N. Mishra⁴⁹, T. Mishra⁵⁸, D. Miśkowiec¹⁰⁰, J. Mitra¹³⁷, C.M. Mitu⁵⁹, N. Mohammadi⁵⁴, B. Mohanty⁸¹,
 L. Molnar¹¹⁶, E. Montes¹⁰, D.A. Moreira De Godoy⁶², L.A.P. Moreno², S. Moretto²⁹, A. Morreale¹¹⁶,
 A. Morsch³⁵, V. Muccifora⁷⁴, E. Mudnic¹¹⁹, D. Mühlheim⁶², S. Muhuri¹³⁷, M. Mukherjee¹³⁷, J.D. Mulligan¹⁴¹,
 M.G. Munhoz¹²³, K. Munning⁴⁵, R.H. Munzer^{97,36,61}, H. Murakami¹³¹, S. Murray⁶⁷, L. Musa³⁵, J. Musinsky⁵⁶,
 C.J. Myers¹²⁶, B. Naik⁴⁸, R. Nair⁷⁹, B.K. Nandi⁴⁸, R. Nania¹⁰⁷, E. Nappi¹⁰⁶, M.U. Naru¹⁶, H. Natal da Luz¹²³,
 C. Nattrass¹²⁹, S.R. Navarro², K. Nayak⁸¹, R. Nayak⁴⁸, T.K. Nayak¹³⁷, S. Nazarenko¹⁰², A. Nedosekin⁵⁵,
 R.A. Negrao De Oliveira³⁵, L. Nellen⁶³, F. Ng¹²⁶, M. Nicassio¹⁰⁰, M. Niculescu⁵⁹, J. Niedziela³⁵,
 B.S. Nielsen⁸³, S. Nikolaev⁸², S. Nikulin⁸², V. Nikulin⁸⁸, F. Noferini^{12,107}, P. Nomokonov⁶⁸, G. Nooren⁵⁴,
 J.C.C. Noris², J. Norman¹²⁸, A. Nyanin⁸², J. Nystrand²², H. Oeschler⁹⁶, S. Oh¹⁴¹, A. Ohlson³⁵, T. Okubo⁴⁷,
 L. Olah¹⁴⁰, J. Olińczak¹³⁸, A.C. Oliveira Da Silva¹²³, M.H. Oliver¹⁴¹, J. Onderwaater¹⁰⁰, C. Oppedisano¹¹³,
 R. Orava⁴⁶, M. Oravec¹¹⁸, A. Ortiz Velasquez⁶³, A. Oskarsson³⁴, J. Otwinowski¹²⁰, K. Oyama⁷⁸, M. Ozdemir⁶¹,
 Y. Pachmayer⁹⁶, V. Pacik⁸³, D. Pagano^{26,135}, P. Pagano³⁰, G. Paic⁶³, S.K. Pal¹³⁷, P. Palni⁷, J. Pan¹³⁹,
 A.K. Pandey⁴⁸, V. Papikyan¹, G.S. Pappalardo¹⁰⁹, P. Pareek⁴⁹, J. Park⁵¹, W.J. Park¹⁰⁰, S. Parmar⁹⁰,
 A. Passfeld⁶², V. Paticchio¹⁰⁶, R.N. Patra¹³⁷, B. Paul¹¹³, H. Pei⁷, T. Peitzmann⁵⁴, X. Peng⁷, H. Pereira Da
 Costa¹⁵, D. Peresunko^{82,77}, E. Perez Lezama⁶¹, V. Peskov⁶¹, Y. Pestov⁵, V. Petráček³⁹, V. Petrov¹¹⁴,
 M. Petrovici⁸⁰, C. Petta²⁸, S. Piano¹¹², M. Pikna³⁸, P. Pillot¹¹⁶, L.O.D.L. Pimentel⁸³, O. Pinazza^{107,35},
 L. Pinsky¹²⁶, D.B. Piyarathna¹²⁶, M. Płoskoń⁷⁶, M. Planinic¹³³, J. Pluta¹³⁸, S. Pochybova¹⁴⁰,
 P.L.M. Podesta-Lerma¹²², M.G. Poghosyan⁸⁷, B. Polichtchouk¹¹⁴, N. Poljak¹³³, W. Poonsawat¹¹⁷, A. Pop⁸⁰,
 H. Poppenborg⁶², S. Porteboeuf-Houssais⁷², J. Porter⁷⁶, J. Pospisil⁸⁶, S.K. Prasad⁴, R. Preghenella^{107,35},
 F. Prino¹¹³, C.A. Pruneau¹³⁹, I. Pshenichnov⁵³, M. Puccio²⁶, G. Puddu²⁴, P. Pujahari¹³⁹, V. Punin¹⁰²,
 J. Putschke¹³⁹, H. Qvigstad²¹, A. Rachevski¹¹², S. Raha⁴, S. Rajput⁹³, J. Rak¹²⁷, A. Rakotozafindrabe¹⁵,
 L. Ramello³², F. Rami⁶⁶, D.B. Rana¹²⁶, R. Raniwala⁹⁴, S. Raniwala⁹⁴, S.S. Räsänen⁴⁶, B.T. Rascanu⁶¹,
 D. Rathee⁹⁰, V. Ratza⁴⁵, I. Ravasenga²⁶, K.F. Read^{129,87}, K. Redlich⁷⁹, A. Rehman²², P. Reichelt⁶¹,
 F. Reidt^{96,35}, X. Ren⁷, R. Renfordt⁶¹, A.R. Reolon⁷⁴, A. Reshetin⁵³, K. Reygers⁹⁶, V. Riabov⁸⁸, R.A. Ricci⁷⁵,
 T. Richert^{34,54}, M. Richter²¹, P. Riedler³⁵, W. Riegler³⁵, F. Riggi²⁸, C. Ristea⁵⁹, M. Rodríguez Cahuanti²,
 K. Røed²¹, E. Rogochaya⁶⁸, D. Rohr⁴², D. Röhrich²², F. Ronchetti^{74,35}, L. Ronflette¹¹⁶, P. Rosnet⁷², A. Rossi²⁹,
 F. Roukoutakis⁹¹, A. Roy⁴⁹, C. Roy⁶⁶, P. Roy¹⁰³, A.J. Rubio Montero¹⁰, R. Rui²⁵, R. Russo²⁶, E. Ryabinkin⁸²,

Y. Ryabov⁸⁸, A. Rybicki¹²⁰, S. Saarinen⁴⁶, S. Sadhu¹³⁷, S. Sadovsky¹¹⁴, K. Šafařík³⁵, B. Sahlmuller⁶¹, B. Sahoo⁴⁸, P. Sahoo⁴⁹, R. Sahoo⁴⁹, S. Sahoo⁵⁸, P.K. Sahu⁵⁸, J. Saini¹³⁷, S. Sakai^{132,74}, M.A. Saleh¹³⁹, J. Salzwedel¹⁹, S. Sambyal⁹³, V. Samsonov^{88,77}, A. Sandoval⁶⁵, M. Sano¹³², D. Sarkar¹³⁷, N. Sarkar¹³⁷, P. Sarma⁴⁴, M.H.P. Sas⁵⁴, E. Scapparone¹⁰⁷, F. Scarlassara²⁹, R.P. Scharenberg⁹⁸, C. Schiaua⁸⁰, R. Schicker⁹⁶, C. Schmidt¹⁰⁰, H.R. Schmidt⁹⁵, M. Schmidt⁹⁵, J. Schukraft³⁵, Y. Schutz^{35,66,116}, K. Schwarz¹⁰⁰, K. Schweda¹⁰⁰, G. Scioli²⁷, E. Scomparin¹¹³, R. Scott¹²⁹, M. Šefčík⁴⁰, J.E. Seger⁸⁹, Y. Sekiguchi¹³¹, D. Sekihata⁴⁷, I. Selyuzhenkov¹⁰⁰, K. Senosi⁶⁷, S. Senyukov^{3,35}, E. Serradilla^{10,65}, P. Sett⁴⁸, A. Sevcenco⁵⁹, A. Shabanov⁵³, A. Shabetai¹¹⁶, O. Shadura³, R. Shahoyan³⁵, A. Shangaraev¹¹⁴, A. Sharma⁹³, A. Sharma⁹⁰, M. Sharma⁹³, M. Sharma⁹³, N. Sharma^{90,129}, A.I. Sheikh¹³⁷, K. Shigaki⁴⁷, Q. Shou⁷, K. Shtejer^{26,9}, Y. Sibiriyak⁸², S. Siddhanta¹⁰⁸, K.M. Sielewicz³⁵, T. Siemiarz⁷⁹, D. Silvermyr³⁴, C. Silvestre⁷³, G. Simatovic¹³³, G. Simonetti³⁵, R. Singaraju¹³⁷, R. Singh⁸¹, V. Singhal¹³⁷, T. Sinha¹⁰³, B. Sitar³⁸, M. Sitta³², T.B. Skaali²¹, M. Slupecki¹²⁷, N. Smirnov¹⁴¹, R.J.M. Snellings⁵⁴, T.W. Snellman¹²⁷, J. Song⁹⁹, M. Song¹⁴², Z. Song⁷, F. Soramel²⁹, S. Sorensen¹²⁹, F. Sozzi¹⁰⁰, E. Spiriti⁷⁴, I. Sputowska¹²⁰, B.K. Srivastava⁹⁸, J. Stachel⁹⁶, I. Stan⁵⁹, P. Stankus⁸⁷, E. Stenlund³⁴, G. Steyn⁶⁷, J.H. Stiller⁹⁶, D. Stocco¹¹⁶, P. Strmen³⁸, A.A.P. Suaide¹²³, T. Sugitate⁴⁷, C. Suire⁵², M. Suleymanov¹⁶, M. Suljic²⁵, R. Sultanov⁵⁵, M. Šumbera⁸⁶, S. Sumowidagdo⁵⁰, K. Suzuki¹¹⁵, S. Swain⁵⁸, A. Szabo³⁸, I. Szarka³⁸, A. Szczepankiewicz¹³⁸, M. Szymanski¹³⁸, U. Tabassam¹⁶, J. Takahashi¹²⁴, G.J. Tambave²², N. Tanaka¹³², M. Tarhini⁵², M. Tariq¹⁸, M.G. Tarzila⁸⁰, A. Tauro³⁵, G. Tejada Muñoz², A. Telesca³⁵, K. Terasaki¹³¹, C. Terrevoli²⁹, B. Teyssier¹³⁴, D. Thakur⁴⁹, D. Thomas¹²¹, R. Tieulent¹³⁴, A. Tikhonov⁵³, A.R. Timmins¹²⁶, A. Toia⁶¹, S. Tripathy⁴⁹, S. Trogolo²⁶, G. Trombetta³³, V. Trubnikov³, W.H. Trzaska¹²⁷, T. Tsuji¹³¹, A. Tumkin¹⁰², R. Turrisi¹¹⁰, T.S. Tveter²¹, K. Ullaland²², E.N. Umaka¹²⁶, A. Uras¹³⁴, G.L. Usai²⁴, A. Utrobicic¹³³, M. Vala⁵⁶, J. Van Der Maarel⁵⁴, J.W. Van Hoorne³⁵, M. van Leeuwen⁵⁴, T. Vanat⁸⁶, P. Vande Vyvre³⁵, D. Varga¹⁴⁰, A. Vargas², M. Vargyas¹²⁷, R. Varma⁴⁸, M. Vasileiou⁹¹, A. Vasiliev⁸², A. Vauthier⁷³, O. Vázquez Doce^{97,36}, V. Vechernin¹³⁶, A.M. Veen⁵⁴, A. Velure²², E. Vercellin²⁶, S. Vergara Limón², R. Vernet⁸, R. Vértesi¹⁴⁰, L. Vickovic¹¹⁹, S. Vigolo⁵⁴, J. Viinikainen¹²⁷, Z. Vilakazi¹³⁰, O. Villalobos Baillie¹⁰⁴, A. Villatoro Tello², A. Vinogradov⁸², L. Vinogradov¹³⁶, T. Virgili³⁰, V. Vislavicius³⁴, A. Vodopyanov⁶⁸, M.A. Völkl⁹⁶, K. Voloshin⁵⁵, S.A. Voloshin¹³⁹, G. Volpe^{33,140}, B. von Haller³⁵, I. Vorobyev^{36,97}, D. Vosecek¹¹⁸, D. Vranic^{35,100}, J. Vrláková⁴⁰, B. Wagner²², J. Wagner¹⁰⁰, H. Wang⁵⁴, M. Wang⁷, D. Watanabe¹³², Y. Watanabe¹³¹, M. Weber¹¹⁵, S.G. Weber¹⁰⁰, D.F. Weiser⁹⁶, J.P. Wessels⁶², U. Westerhoff⁶², A.M. Whitehead⁹², J. Wiechula⁶¹, J. Wikne²¹, G. Wilk⁷⁹, J. Wilkinson⁹⁶, G.A. Willems⁶², M.C.S. Williams¹⁰⁷, B. Windelband⁹⁶, M. Winn⁹⁶, S. Yalcin⁷¹, P. Yang⁷, S. Yano⁴⁷, Z. Yin⁷, H. Yokoyama^{73,132}, I.-K. Yoo^{35,99}, J.H. Yoon⁵¹, V. Yurchenko³, V. Zaccaro⁸³, A. Zaman¹⁶, C. Zampolli^{35,107}, H.J.C. Zanoli¹²³, S. Zaporozhets⁶⁸, N. Zardoshti¹⁰⁴, A. Zarochentsev¹³⁶, P. Závada⁵⁷, N. Zaviyalov¹⁰², H. Zbroszczyk¹³⁸, M. Zhalov⁸⁸, H. Zhang^{7,22}, X. Zhang^{76,7}, Y. Zhang⁷, C. Zhang⁵⁴, Z. Zhang⁷, C. Zhao²¹, N. Zhigareva⁵⁵, D. Zhou⁷, Y. Zhou⁸³, Z. Zhou²², H. Zhu^{22,7}, J. Zhu^{116,7}, A. Zichichi^{27,12}, A. Zimmermann⁹⁶, M.B. Zimmermann^{35,62}, G. Zinovjev³, J. Zmeskal¹¹⁵

Affiliation notes

ⁱ Deceased

ⁱⁱ Also at: Georgia State University, Atlanta, Georgia, United States

ⁱⁱⁱ Also at: Also at Department of Applied Physics, Aligarh Muslim University, Aligarh, India

^{iv} Also at: M.V. Lomonosov Moscow State University, D.V. Skobeltsyn Institute of Nuclear, Physics, Moscow, Russia

Collaboration Institutes

¹A.I. Alikhanyan National Science Laboratory (Yerevan Physics Institute) Foundation, Yerevan, Armenia

²Benemérita Universidad Autónoma de Puebla, Puebla, Mexico

³Bogolyubov Institute for Theoretical Physics, Kiev, Ukraine

⁴Bose Institute, Department of Physics and Centre for Astroparticle Physics and Space Science (CAPSS), Kolkata, India

⁵Budker Institute for Nuclear Physics, Novosibirsk, Russia

⁶California Polytechnic State University, San Luis Obispo, California, United States

⁷Central China Normal University, Wuhan, China

⁸Centre de Calcul de l'IN2P3, Villeurbanne, Lyon, France

⁹Centro de Aplicaciones Tecnológicas y Desarrollo Nuclear (CEADEN), Havana, Cuba

- ¹⁰Centro de Investigaciones Energéticas Medioambientales y Tecnológicas (CIEMAT), Madrid, Spain
- ¹¹Centro de Investigación y de Estudios Avanzados (CINVESTAV), Mexico City and Mérida, Mexico
- ¹²Centro Fermi - Museo Storico della Fisica e Centro Studi e Ricerche “Enrico Fermi”, Rome, Italy
- ¹³Chicago State University, Chicago, Illinois, United States
- ¹⁴China Institute of Atomic Energy, Beijing, China
- ¹⁵Commissariat à l’Energie Atomique, IRFU, Saclay, France
- ¹⁶COMSATS Institute of Information Technology (CIIT), Islamabad, Pakistan
- ¹⁷Departamento de Física de Partículas and IGFAE, Universidad de Santiago de Compostela, Santiago de Compostela, Spain
- ¹⁸Department of Physics, Aligarh Muslim University, Aligarh, India
- ¹⁹Department of Physics, Ohio State University, Columbus, Ohio, United States
- ²⁰Department of Physics, Sejong University, Seoul, South Korea
- ²¹Department of Physics, University of Oslo, Oslo, Norway
- ²²Department of Physics and Technology, University of Bergen, Bergen, Norway
- ²³Dipartimento di Fisica dell’Università ‘La Sapienza’ and Sezione INFN, Rome, Italy
- ²⁴Dipartimento di Fisica dell’Università and Sezione INFN, Cagliari, Italy
- ²⁵Dipartimento di Fisica dell’Università and Sezione INFN, Trieste, Italy
- ²⁶Dipartimento di Fisica dell’Università and Sezione INFN, Turin, Italy
- ²⁷Dipartimento di Fisica e Astronomia dell’Università and Sezione INFN, Bologna, Italy
- ²⁸Dipartimento di Fisica e Astronomia dell’Università and Sezione INFN, Catania, Italy
- ²⁹Dipartimento di Fisica e Astronomia dell’Università and Sezione INFN, Padova, Italy
- ³⁰Dipartimento di Fisica ‘E.R. Caianiello’ dell’Università and Gruppo Collegato INFN, Salerno, Italy
- ³¹Dipartimento DISAT del Politecnico and Sezione INFN, Turin, Italy
- ³²Dipartimento di Scienze e Innovazione Tecnologica dell’Università del Piemonte Orientale and INFN Sezione di Torino, Alessandria, Italy
- ³³Dipartimento Interateneo di Fisica ‘M. Merlin’ and Sezione INFN, Bari, Italy
- ³⁴Division of Experimental High Energy Physics, University of Lund, Lund, Sweden
- ³⁵European Organization for Nuclear Research (CERN), Geneva, Switzerland
- ³⁶Excellence Cluster Universe, Technische Universität München, Munich, Germany
- ³⁷Faculty of Engineering, Bergen University College, Bergen, Norway
- ³⁸Faculty of Mathematics, Physics and Informatics, Comenius University, Bratislava, Slovakia
- ³⁹Faculty of Nuclear Sciences and Physical Engineering, Czech Technical University in Prague, Prague, Czech Republic
- ⁴⁰Faculty of Science, P.J. Šafárik University, Košice, Slovakia
- ⁴¹Faculty of Technology, Buskerud and Vestfold University College, Tonsberg, Norway
- ⁴²Frankfurt Institute for Advanced Studies, Johann Wolfgang Goethe-Universität Frankfurt, Frankfurt, Germany
- ⁴³Gangneung-Wonju National University, Gangneung, South Korea
- ⁴⁴Gauhati University, Department of Physics, Guwahati, India
- ⁴⁵Helmholtz-Institut für Strahlen- und Kernphysik, Rheinische Friedrich-Wilhelms-Universität Bonn, Bonn, Germany
- ⁴⁶Helsinki Institute of Physics (HIP), Helsinki, Finland
- ⁴⁷Hiroshima University, Hiroshima, Japan
- ⁴⁸Indian Institute of Technology Bombay (IIT), Mumbai, India
- ⁴⁹Indian Institute of Technology Indore, Indore, India
- ⁵⁰Indonesian Institute of Sciences, Jakarta, Indonesia
- ⁵¹Inha University, Incheon, South Korea
- ⁵²Institut de Physique Nucléaire d’Orsay (IPNO), Université Paris-Sud, CNRS-IN2P3, Orsay, France
- ⁵³Institute for Nuclear Research, Academy of Sciences, Moscow, Russia
- ⁵⁴Institute for Subatomic Physics of Utrecht University, Utrecht, Netherlands
- ⁵⁵Institute for Theoretical and Experimental Physics, Moscow, Russia
- ⁵⁶Institute of Experimental Physics, Slovak Academy of Sciences, Košice, Slovakia
- ⁵⁷Institute of Physics, Academy of Sciences of the Czech Republic, Prague, Czech Republic
- ⁵⁸Institute of Physics, Bhubaneswar, India
- ⁵⁹Institute of Space Science (ISS), Bucharest, Romania
- ⁶⁰Institut für Informatik, Johann Wolfgang Goethe-Universität Frankfurt, Frankfurt, Germany
- ⁶¹Institut für Kernphysik, Johann Wolfgang Goethe-Universität Frankfurt, Frankfurt, Germany

- ⁶²Institut für Kernphysik, Westfälische Wilhelms-Universität Münster, Münster, Germany
- ⁶³Instituto de Ciencias Nucleares, Universidad Nacional Autónoma de México, Mexico City, Mexico
- ⁶⁴Instituto de Física, Universidade Federal do Rio Grande do Sul (UFRGS), Porto Alegre, Brazil
- ⁶⁵Instituto de Física, Universidad Nacional Autónoma de México, Mexico City, Mexico
- ⁶⁶Institut Pluridisciplinaire Hubert Curien (IPHC), Université de Strasbourg, CNRS-IN2P3, Strasbourg, France, Strasbourg, France
- ⁶⁷iThemba LABS, National Research Foundation, Somerset West, South Africa
- ⁶⁸Joint Institute for Nuclear Research (JINR), Dubna, Russia
- ⁶⁹Konkuk University, Seoul, South Korea
- ⁷⁰Korea Institute of Science and Technology Information, Daejeon, South Korea
- ⁷¹KTO Karatay University, Konya, Turkey
- ⁷²Laboratoire de Physique Corpusculaire (LPC), Clermont Université, Université Blaise Pascal, CNRS-IN2P3, Clermont-Ferrand, France
- ⁷³Laboratoire de Physique Subatomique et de Cosmologie, Université Grenoble-Alpes, CNRS-IN2P3, Grenoble, France
- ⁷⁴Laboratori Nazionali di Frascati, INFN, Frascati, Italy
- ⁷⁵Laboratori Nazionali di Legnaro, INFN, Legnaro, Italy
- ⁷⁶Lawrence Berkeley National Laboratory, Berkeley, California, United States
- ⁷⁷Moscow Engineering Physics Institute, Moscow, Russia
- ⁷⁸Nagasaki Institute of Applied Science, Nagasaki, Japan
- ⁷⁹National Centre for Nuclear Studies, Warsaw, Poland
- ⁸⁰National Institute for Physics and Nuclear Engineering, Bucharest, Romania
- ⁸¹National Institute of Science Education and Research, Bhubaneswar, India
- ⁸²National Research Centre Kurchatov Institute, Moscow, Russia
- ⁸³Niels Bohr Institute, University of Copenhagen, Copenhagen, Denmark
- ⁸⁴Nikhef, Nationaal instituut voor subatomaire fysica, Amsterdam, Netherlands
- ⁸⁵Nuclear Physics Group, STFC Daresbury Laboratory, Daresbury, United Kingdom
- ⁸⁶Nuclear Physics Institute, Academy of Sciences of the Czech Republic, Řež u Prahy, Czech Republic, Řež u Prahy, Czech Republic
- ⁸⁷Oak Ridge National Laboratory, Oak Ridge, Tennessee, United States
- ⁸⁸Petersburg Nuclear Physics Institute, Gatchina, Russia
- ⁸⁹Physics Department, Creighton University, Omaha, Nebraska, United States
- ⁹⁰Physics Department, Panjab University, Chandigarh, India
- ⁹¹Physics Department, University of Athens, Athens, Greece
- ⁹²Physics Department, University of Cape Town, Cape Town, South Africa
- ⁹³Physics Department, University of Jammu, Jammu, India
- ⁹⁴Physics Department, University of Rajasthan, Jaipur, India
- ⁹⁵Physikalisches Institut, Eberhard Karls Universität Tübingen, Tübingen, Germany
- ⁹⁶Physikalisches Institut, Ruprecht-Karls-Universität Heidelberg, Heidelberg, Germany
- ⁹⁷Physik Department, Technische Universität München, Munich, Germany
- ⁹⁸Purdue University, West Lafayette, Indiana, United States
- ⁹⁹Pusan National University, Pusan, South Korea
- ¹⁰⁰Research Division and ExtreMe Matter Institute EMMI, GSI Helmholtzzentrum für Schwerionenforschung, Darmstadt, Germany
- ¹⁰¹Rudjer Bošković Institute, Zagreb, Croatia
- ¹⁰²Russian Federal Nuclear Center (VNIIEF), Sarov, Russia
- ¹⁰³Saha Institute of Nuclear Physics, Kolkata, India
- ¹⁰⁴School of Physics and Astronomy, University of Birmingham, Birmingham, United Kingdom
- ¹⁰⁵Sección Física, Departamento de Ciencias, Pontificia Universidad Católica del Perú, Lima, Peru
- ¹⁰⁶Sezione INFN, Bari, Italy
- ¹⁰⁷Sezione INFN, Bologna, Italy
- ¹⁰⁸Sezione INFN, Cagliari, Italy
- ¹⁰⁹Sezione INFN, Catania, Italy
- ¹¹⁰Sezione INFN, Padova, Italy
- ¹¹¹Sezione INFN, Rome, Italy
- ¹¹²Sezione INFN, Trieste, Italy

- ¹¹³Sezione INFN, Turin, Italy
- ¹¹⁴SSC IHEP of NRC Kurchatov institute, Protvino, Russia
- ¹¹⁵Stefan Meyer Institut für Subatomare Physik (SMI), Vienna, Austria
- ¹¹⁶SUBATECH, Ecole des Mines de Nantes, Université de Nantes, CNRS-IN2P3, Nantes, France
- ¹¹⁷Suranaree University of Technology, Nakhon Ratchasima, Thailand
- ¹¹⁸Technical University of Košice, Košice, Slovakia
- ¹¹⁹Technical University of Split FESB, Split, Croatia
- ¹²⁰The Henryk Niewodniczanski Institute of Nuclear Physics, Polish Academy of Sciences, Cracow, Poland
- ¹²¹The University of Texas at Austin, Physics Department, Austin, Texas, United States
- ¹²²Universidad Autónoma de Sinaloa, Culiacán, Mexico
- ¹²³Universidade de São Paulo (USP), São Paulo, Brazil
- ¹²⁴Universidade Estadual de Campinas (UNICAMP), Campinas, Brazil
- ¹²⁵Universidade Federal do ABC, Santo Andre, Brazil
- ¹²⁶University of Houston, Houston, Texas, United States
- ¹²⁷University of Jyväskylä, Jyväskylä, Finland
- ¹²⁸University of Liverpool, Liverpool, United Kingdom
- ¹²⁹University of Tennessee, Knoxville, Tennessee, United States
- ¹³⁰University of the Witwatersrand, Johannesburg, South Africa
- ¹³¹University of Tokyo, Tokyo, Japan
- ¹³²University of Tsukuba, Tsukuba, Japan
- ¹³³University of Zagreb, Zagreb, Croatia
- ¹³⁴Université de Lyon, Université Lyon 1, CNRS/IN2P3, IPN-Lyon, Villeurbanne, Lyon, France
- ¹³⁵Università di Brescia, Brescia, Italy
- ¹³⁶V. Fock Institute for Physics, St. Petersburg State University, St. Petersburg, Russia
- ¹³⁷Variable Energy Cyclotron Centre, Kolkata, India
- ¹³⁸Warsaw University of Technology, Warsaw, Poland
- ¹³⁹Wayne State University, Detroit, Michigan, United States
- ¹⁴⁰Wigner Research Centre for Physics, Hungarian Academy of Sciences, Budapest, Hungary
- ¹⁴¹Yale University, New Haven, Connecticut, United States
- ¹⁴²Yonsei University, Seoul, South Korea
- ¹⁴³Zentrum für Technologietransfer und Telekommunikation (ZTT), Fachhochschule Worms, Worms, Germany